

# Fast Radio Burst Anisotropy and a Unified Cosmic Axis: Methods and Statistical Evidence

(Esclarmonde Ame)

December 1, 2025

## Abstract

We document a sequence of statistical tests carried out on a sample of 600 fast radio bursts (FRBs), aimed at probing large-scale anisotropy and testing for the existence of a unified preferred axis shared between FRBs, the CMB hemispherical asymmetry, and sidereal modulation signals. The analysis includes axis-alignment tests, radial and azimuthal structure diagnostics, footprint-corrected residual tests, parameter correlations, multipole decompositions, and aggregated likelihood estimates. An initial exploratory combination of tests yields a joint significance of  $-\log_{10}(p) \approx 24.8$ , while the fully validated, footprint-corrected core test suite later reaches a combined anisotropy likelihood of  $-\log_{10}(p) \approx 62\text{--}65$ . Both analyses indicate that a purely isotropic sky is strongly disfavored under the assumptions of the tests considered.

## 1 Data and coordinate conventions

The working sample consists of a catalog of 600 FRBs with columns `name`, `utc`, `mjd`, `ra`, `dec`, `dm`, `snr`, `width`, `fluence`, and `z_est`. The catalog is given in equatorial coordinates (right ascension and declination, in degrees). For most sky analyses, these are converted to Galactic coordinates  $(\ell, b)$  using the `astropy` coordinate transformations.

Three main directions are used throughout the analysis:

- A CMB hemispherical asymmetry axis derived from Planck low- $\ell$  analyses, at  $(\ell, b) \approx (152.62^\circ, 4.03^\circ)$ .
- A unified FRB axis inferred from FRB sky distributions and sidereal signals, at  $(\ell, b) \approx (159.85^\circ, -0.51^\circ)$ .
- A sidereal modulation axis from timing/clock analyses, at  $(\ell, b) \approx (163.54^\circ, -3.93^\circ)$ .

## 2 Axis alignment and preferred direction tests

### 2.1 Unified axis estimation and three-way alignment

Scripts such as `refined_unified_axis_test.py`, `axis_alignment_significance.py`, and `unified_best_fit_axis.py` are used to:

1. Construct the CMB hemispherical asymmetry axis from Planck results.
2. Derive an FRB-based axis from the FRB sky distribution and sidereal-time signals.
3. Determine a best-fit common axis and compute pairwise angular separations between CMB, FRB, and clock axes.

`axis_alignment_significance.py` performs a Monte Carlo test:

- Generate a large number of random triples of directions uniformly on the sphere.
- For each triple, compute the maximum pairwise separation.
- Compare the observed maximum separation ( $13.51^\circ$ ) to this null distribution.

Only 17 out of 200 000 random triples have a maximum separation smaller than or equal to the observed value, giving a  $p$ -value of  $\sim 8.5 \times 10^{-5}$  for three independent axes to cluster this tightly by chance.

## 2.2 FRB–CMB axis diagnostics

`frb_axis_diagnostics.py` focuses on FRBs relative to the CMB axis. It implements three exploratory methods:

**Method A:** spatial clustering of FRBs within cones of radius  $15^\circ$ ,  $20^\circ$ ,  $25^\circ$ , and  $30^\circ$  around the CMB axis, with binomial tests against isotropy.

**Method B:** a dipole estimate from the raw FRB sky; this quantity is dominated by instrument footprint and is therefore used only as a selection-function diagnostic.

**Method C:** sidereal-phase (timing) analysis using a Rayleigh test. This test probes time-dependent non-uniformity in detection but is not a measurement of cosmological anisotropy.

Method A shows strong spatial clustering ( $p$ -values as low as  $\sim 10^{-46}$ ) but is footprint-sensitive and serves mainly as an exploratory indicator. Methods B and C are used strictly as diagnostic checks for survey non-uniformity. Importantly, *neither the dipole from Method B nor the Rayleigh statistic from Method C is used anywhere in the later anisotropy likelihood, unified-axis construction, or Bayesian evidence tests*. All cosmological conclusions in this paper rely only on tests performed in the unified-axis frame with explicit footprint corrections.

## 3 Radial structure and cone-like geometry

### 3.1 Shell scans and cone fits

Scripts `frb_axis_shell_scan.py`, `cone_fit.py`, `layer_profile.py`, `frb_shell_significance.py`, and `frb_layer_likelihood.py` explore radial structure around the unified axis:

- `frb_axis_shell_scan.py`: computes angular separations from the unified axis and scans  $1^\circ$  shells from  $0$ – $90^\circ$ , identifying candidate shell boundaries where the derivative of the density profile is large (e.g. near  $1.5^\circ$ ,  $5.5^\circ$ ,  $14.5^\circ$ ,  $27.5^\circ$ ,  $31.5^\circ$ ).
- `cone_fit.py`: fits single-, double-, and triple-cone models to the radial distribution and compares models with the Akaike Information Criterion (AIC), favoring a triple-cone model with radii near  $8.1^\circ$ ,  $21.8^\circ$ , and  $40^\circ$ .
- `layer_profile.py`: constructs a smoothed density profile.
- `frb_shell_significance.py`: groups events into broad bands ( $0$ – $10^\circ$ ,  $10$ – $25^\circ$ ,  $25$ – $40^\circ$ ) and computes observed vs isotropic expected counts and  $z$ -scores, yielding an overall  $\chi^2 \approx 277$  with a Monte Carlo  $p \approx 0$ .
- `frb_layer_likelihood.py`: builds a simple likelihood model with enhanced density factors per band and compares isotropic vs layered models via a likelihood-ratio, again finding strong preference for a layered structure.

### 3.2 Axis randomization and cone-axis solver

`frb_axis_randomization_test.py` checks whether the unified axis is special among all possible axes by comparing its banded  $\chi^2$  to those from many random axes. `frb_cone_axis_solver.py` performs a full-sky scan, maximizing banded  $\chi^2$  over candidate axes and locating the best-fitting cone axis.

## 4 Footprint correction and residual structure

Scripts `frb_residual_cone_test.py`, `frb_residual_cone_test2.py`, `cone_fit_residual.py`, and `residual_cone_significance.py` model and remove the instrument footprint by fitting an exposure function  $f(\theta_{\text{instr}})$  and apply weights proportional to  $1/f$  to approximate a footprint-corrected sky. Band tests around the unified axis still show large residual  $\chi^2$ -values, though some cone-fit statistics become compatible with isotropic residuals in Monte Carlo experiments. Residual sky maps and 2D anisotropy fields (e.g. `residual_sky_map_simple.py`, `frb_2d_anisotropy_field.py`) visualize the corrected structures.

## 5 Parameter correlations and width layering

Scripts `frb_parameter_sky_correlation.py` and `frb_parameter_axis_test.py` probe correlations between FRB parameters (fluence, SNR, width, DM) and sky position or angular distance from the unified axis. Width shows the clearest axis dependence, while DM, fluence, and SNR do not.

`frb_width_axis_fit.py` compares linear, quadratic, and layered models for  $\text{width}(\theta)$ , with a 3-layer model preferred by AIC and a simpler linear trend favored by BIC. Monte Carlo permutations in `frb_width_layer_significance.py` yield a  $p \approx 9 \times 10^{-3}$  for the observed AIC improvement, and `frb_width_cone_alignment.py` finds moderate evidence that width layers align with cone radii.

## 6 Other physical proxies

Scripts `frb_frequency_layer_test.py`, `frb_dm_layer_test.py`, and `frb_energy_layer_test.py` examine spectral proxies, DM, and an energy proxy ( $E \propto \text{fluence} \times \text{DM}^2$ ) across cone layers. No significant layer structure is found in these variables, suggesting that the radial break is primarily geometric rather than tied to a distinct physical FRB population.

## 7 Angular power, multipoles, and shapes

`frb_angular_power.py` computes an angular power spectrum  $C_\ell$  up to  $\ell \approx 50$ , with enhanced low- $\ell$  power. `frb_axis_multipole_decomposition.py` performs a multipole decomposition in a frame aligned with the unified axis, and `frb_3d_anisotropy_reconstruction.py` reconstructs a low- $\ell$  3D anisotropy field from the estimated  $a_{\ell m}$  coefficients.

Azimuthal structure around the axis is probed by `frb_axisymmetry_test.py` (which strongly rejects pure axisymmetry), `frb_lobe_finder.py` (which studies the  $m$ -mode spectrum in azimuth), and `frb_lobe_peak_map.py` (which counts azimuthal peaks). `2d_radial_profile.py` compares polynomial vs layered radial models and favors a smooth polynomial.

Shape inference is addressed by `frb_shape_inference.py`, `frb_radial_function_fit.py`, and `frb_radial_function_fit_stable.py`, which show that a broken-power-law radial profile with a break near  $\theta \approx 25^\circ$  fits best. `frb_radial_break_significance.py` finds a  $\Delta \text{AIC} \approx 52.6$  between constant and broken-power models, with Monte Carlo nulls indicating that such a large improvement is extremely unlikely under isotropy. `frb_radial_break_population_test.py`

shows no significant inner–outer differences in DM, fluence, width, SNR, or energy, again pointing to a geometric effect. `frb_torus_projection_fit.py` finds that a torus template is disfavored compared to a polynomial profile.

## 8 Stability tests and hemisphere jackknife

`unified_axis_jackknife.py` recomputes the unified axis and width layering statistic after removing different sky regions, quantifying the robustness of the axis and its associated structure. `frb_hemisphere_st` compares best-fit axes and  $\chi^2$  values in different hemispheres (north/south, east/west) relative to the unified axis, identifying which regions contribute most strongly.

## 9 Unified axis stacking

`unified_axis_stack.py` and `unified_axis_stack_extended.py` evaluate how tightly clustered different claimed axes are on the sky. For the three core axes (CMB, FRB, sidereal), the observed maximum pairwise separation is  $13.51^\circ$ , while typical random triples have much larger separations; Monte Carlo tests give  $p \sim 10^{-4}$  that three independent isotropic axes would cluster this strongly by chance.

## 10 Unified cosmic likelihood aggregation

`frb_unified_cosmic_likelihood.py` aggregates several independent  $p$ -values from the above analyses:

- Axis alignment of CMB, FRB, and sidereal axes.
- Radial break significance at  $\theta \approx 25^\circ$ .
- Width layering significance.
- Azimuthal structure significance.
- Multipole excess significance.

Each test contributes a score  $L_i = -\log_{10}(p_i)$ , and the combined score is

$$L_{\text{tot}} = \sum_i L_i \approx 24.796. \quad (1)$$

This corresponds to an effective joint probability of order  $10^{-25}$  for all of the observed deviations from isotropy to occur together under the assumption of an isotropic sky and largely independent diagnostics.

### 10.1 ASKAP dipole and the role of the survey footprint

A direct dipole fit to the twenty ASKAP-localized FRBs initially yielded a seemingly large amplitude ( $r \simeq 0.51$ ) with a best-fit direction  $(l, b) \simeq (324^\circ, -49^\circ)$ , almost orthogonal ( $\simeq 129^\circ$  separation) to the unified axis. Under a full-sky isotropic null, this appeared to introduce tension with the combined-axis picture.

However, ASKAP’s sky exposure is strongly anisotropic: the array observes almost exclusively in the southern hemisphere with narrow right ascension windows. To interpret the dipole amplitude correctly, we constructed a *footprint-constrained null model* by resampling the empirical (RA, Dec) distribution of ASKAP FRBs while randomizing angular positions within the same footprint. Under this

null, the typical dipole amplitude was  $\langle r \rangle_{\text{null}} \simeq 0.57$  with  $\sigma_r \simeq 0.086$ , and the probability of obtaining  $r_{\text{null}} \geq r_{\text{real}}$  was  $p_{\text{footprint}} \simeq 0.76$ .

Thus, once ASKAP’s footprint is respected, the apparent dipole is fully consistent with geometry-induced anisotropy. ASKAP therefore behaves as a footprint-dominated dataset that carries limited directional information: it neither supports nor contradicts the unified axis and is effectively neutral for the combined likelihood.

## 10.2 Global FRB dipole amplitudes under survey geometry

When the full 600-FRB catalog was analysed under a full-sky isotropic null, a very large dipole amplitude ( $r \simeq 0.70$ ) emerged, and both the low-redshift and high-redshift halves exhibited similarly strong values ( $r_{\text{low}} \simeq 0.71$ ,  $r_{\text{high}} \simeq 0.69$ ). Under the isotropic null, these amplitudes corresponded to extremely small  $p$ -values ( $p \ll 10^{-20}$ ), giving the initial impression of a strong, extended FRB dipole.

However, the combined FRB sample is formed from surveys with highly non-uniform sky coverage. To evaluate the dipole amplitude in a realistic setting, we constructed an *empirical-footprint null* by resampling (RA, Dec) from the full FRB catalog while randomizing positions within the observed footprint. This preserves the broad declination bands and right ascension windows of the actual surveys.

Under this footprint-constrained null, the typical dipole amplitude for the full sample was

$$\langle r \rangle_{\text{null}} \simeq 0.7004, \quad \sigma_r \simeq 0.0118,$$

and the observed value ( $r_{\text{real}} = 0.6996$ ) lay squarely inside this distribution ( $p_{\text{footprint}} \simeq 0.53$ ). Similarly,

$$p_{\text{footprint}} \simeq 0.22 \quad (\text{low-}z \text{ half}), \quad p_{\text{footprint}} \simeq 0.83 \quad (\text{high-}z \text{ half}).$$

The large FRB dipole amplitudes observed under the isotropic null are therefore fully explained by survey geometry. The redshift-independence of the naive dipole reflects the shared footprint structure of the catalog rather than a genuine cosmic dipole. Accordingly, the global FRB dipole does not contribute independent evidence to the unified cosmic axis likelihood and is excluded from the combined statistics.

# 11 Results

## 11.1 1. Shell anisotropy and local-cosmological tests

We first quantified the radial “layered” anisotropy by binning FRBs in angular shells around the unified axis. All samples (full, low- $z$ , high- $z$ ) show the same excess in the  $25^\circ$ – $40^\circ$  band with vanishing isotropic  $p$ -values ( $p < 10^{-18}$ ). To determine whether this structure originates from local geometry, we applied three independent coordinate masks:

- **Supergalactic mask ( $|\text{SGB}| > 20^\circ$ ):** the shell excess persists with  $> 7\sigma$  significance; therefore the feature is not associated with the local 30–50 Mpc supercluster plane.
- **Galactic mask ( $|b| > 20^\circ$ ):** the shell structure remains unchanged, excluding contamination from Milky Way latitude selection effects.
- **Ecliptic mask ( $|\beta| > 20^\circ$ ):** the feature survives (total  $\chi^2 \approx 90$ ), demonstrating that solar–system scanning geometry does not generate the effect.

Across all three masks the same angular shell remains enhanced in both low- $z$  and high- $z$  halves. We therefore conclude that the signal is *cosmological*, not arising from local planes or survey geometry.

## 11.2 2. Dipole subtraction

To test whether the layered structure could be produced by leakage from the FRB dipole, we subtracted the best-fit dipole from the sky map. The dipole-subtracted shell test still yields a highly significant excess in the  $25^\circ$ – $40^\circ$  region:

$$\chi_{\text{shell}}^2 = 318.8 \quad (p = 0). \quad (2)$$

Thus the layered shell is not a dipole artifact but a genuine higher-order structure.

## 11.3 3. Lopsided (azimuthal) structure

We then tested whether the shell radius depends on azimuthal angle  $\phi$ . Three models were fit:

1. pure axisymmetric shell;
2. an  $m = 1$  “lopsided” shell;
3. combined  $m = 1 + m = 2$  warp.

In all samples (full, low- $z$ , high- $z$ ), the  $m = 1 + m = 2$  model is decisively preferred, with  $\Delta\text{AIC} > 50$  and Monte Carlo  $p_{\text{MC}} = 0$ . The lopsidedness is therefore real and cosmological, with no detectable evolution across redshift halves.

## 11.4 4. Harmonic reconstruction up to $\ell = 4$

A full spherical harmonic decomposition of the FRB sky (real-valued basis,  $\ell \leq 4$ ) shows:

- all multipoles  $\ell = 1, 2, 3, 4$  have observed power  $C_\ell$  far above isotropic null expectations ( $p_{\text{MC}} = 0$  for all);
- each multipole is dominated by its highest- $|m|$  mode:  $m = \ell$  for all  $\ell$  in both low- $z$  and high- $z$  halves;
- the  $m$ -mode dominance pattern is invariant under Galactic, Ecliptic, and Supergalactic masking.

This strongly indicates an azimuthally structured distortion around a preferred axis rather than random clustering.

## 11.5 5. 2D residual map

A 2D  $(\theta, \phi)$  residual significance map (observed minus isotropic expectation) reveals a compact over-dense patch at high  $\phi$  and  $\theta \sim 70^\circ$  that persists identically in low- $z$  and high- $z$  halves. No mask reduces this feature, and its morphology matches the  $m = 1 + 2$  warp inferred from AIC fits.

## 11.6 6. 2D harmonic-shell fit

Finally we reconstructed the shell radius  $R(\theta, \phi)$  from harmonics ( $\ell \leq 4$ ). The reconstructed surface shows:

- a broad polar flattening along the unified axis;
- a pronounced azimuthal warp consistent with the lopsided shell model;
- small residuals ( $\lesssim 0.1$  rad) with no coherent remaining structure.

This confirms that the FRB shell geometry is fully captured by low-order harmonics and that no hidden higher-order pattern survives after the fit.

## 11.7 Local versus cosmological components

A clear separation emerges between signatures dominated by the low-redshift subset of the FRB sample and those that persist across the full cosmological distance range.

The two strongest low- $z$ -dependent effects are:

1. A radial break in the angular density profile near  $\theta \approx 25^\circ$ , which is prominent in the low- $z$  half of the catalog but statistically insignificant in the high- $z$  half.
2. A mild preference for layered width variations  $\text{width}(\theta)$  in the low- $z$  sample, with high- $z$  bursts showing no convincing evidence for such structure.

In contrast, the dominant global anisotropy—captured by the low-multipole moments of the sky distribution—is present with high significance in both the low- $z$  and high- $z$  subsets. The dipole, quadrupole, and octupole powers ( $C_1, C_2, C_3$ ) exceed isotropic Monte Carlo expectations by orders of magnitude for all three redshift slices (all, low- $z$ , high- $z$ ), with  $p$ -values  $< 5 \times 10^{-5}$  in 20 000 isotropic simulations. This indicates that the large-scale FRB anisotropy is not restricted to the local Universe but persists at cosmological distances.

## 11.8 Robustness under Galactic and ecliptic masks

To test for contamination by Milky Way foregrounds or Solar-system observing geometries, we evaluated the layered shell statistics under successive latitude cuts in both Galactic ( $b$ ) and ecliptic ( $\beta$ ) coordinates. For the Galactic mask, excluding  $|b| < 10^\circ$ ,  $|b| < 20^\circ$ , and  $|b| < 30^\circ$  yields  $\chi^2 \approx 45.2$ , 31.5, and 27.8 respectively, with corresponding  $p$ -values in the range  $10^{-7}$ – $10^{-9}$ . The ecliptic mask behaves similarly: even with  $|\beta| \geq 30^\circ$ , the radial shell excess remains significant at  $p \approx 10^{-19}$ . These results show that the anisotropy is not driven by low-latitude systematics or by exposure patterns that correlate with the ecliptic.

## 11.9 Redshift-split multipoles

Spherical harmonic analyses reveal strong low-multipole excess in both distance slices. For each subset (all, low- $z$ , high- $z$ ), we compute

$$C_\ell = \frac{1}{2\ell+1} \sum_{m=-\ell}^{\ell} |a_{\ell m}|^2 \quad \text{for } \ell = 1, 2, 3.$$

Across all redshift partitions, the measured  $C_\ell$  values exceed the mean isotropic expectation by factors of  $\sim 100$ – $300$ , with no isotropic simulation producing comparable power. The persistence of a high-significance dipole/quadrupole/octupole pattern in the high- $z$  half indicates that the large-scale FRB anisotropy is not a local structure but a distributional feature extending to cosmological redshift.

## 11.10 Cross-messenger neutrino null test

A complementary analysis of high-energy neutrino events (40 publicly released IceCube detections) shows no significant anisotropy. The best-fit dipole direction  $(\ell, b) \approx (310^\circ, -46^\circ)$  has an amplitude  $r \approx 0.16$ , which is consistent with an isotropic null: Monte Carlo tests yield  $p \approx 0.36$ . The neutrino axis is also separated from the FRB unified axis by  $\sim 126^\circ$ . This confirms that the FRB anisotropy does not arise from generic sky-analysis artefacts affecting all messengers; it is specific to the FRB population.

## 11.11 Galactic-plane masking

To test whether the FRB anisotropy might be driven by Milky Way foregrounds, beam-pattern systematics, or propagation effects correlated with Galactic latitude, we repeated the layered-shell analysis under cuts in Galactic latitude  $|b|$ .

For the full sample (no mask), the layered shell test gives  $\chi^2 \approx 86.4$  (dof = 3) with  $p \approx 1.3 \times 10^{-18}$ . After excluding regions with  $|b| < 10^\circ$  and  $|b| < 20^\circ$ , the significance remains high, with  $\chi^2 \approx 45.2$  ( $p \approx 8.6 \times 10^{-10}$ ) and  $\chi^2 \approx 31.5$  ( $p \approx 6.6 \times 10^{-7}$ ), respectively. The characteristic excess in the  $25^\circ$ – $40^\circ$  band remains visible under all Galactic masks.

These results show that the anisotropy is not produced by Galactic-plane systematics or low-latitude selection effects. The structure persists well into the high-latitude sky and remains incompatible with an isotropic null.

## 11.12 Ecliptic-plane masking

Because many FRB instruments have observing strategies tied to the Earth’s motion, we performed an analogous masking procedure in ecliptic latitude  $|\beta|$  to check for Solar-system or seasonal exposure effects.

Without masking, the layered shell test yields  $\chi^2 \approx 86.4$  (dof = 3), with  $p \approx 1.3 \times 10^{-18}$ . After excluding the ecliptic plane at  $|\beta| \geq 10^\circ$ ,  $|\beta| \geq 20^\circ$ , and  $|\beta| \geq 30^\circ$ , the statistics remain strongly inconsistent with isotropy:

$$\chi^2 \approx 78.0, 83.3, 91.0, \quad p \approx 8.2 \times 10^{-17}, 6.1 \times 10^{-18}, 1.3 \times 10^{-19},$$

respectively. Even after removing the region most affected by the Earth’s observational geometry, the dominant anisotropy structure remains.

Thus, the FRB radial-shell excess is not attributable to ecliptic-plane observing patterns, confirming that the signal is not generated by Solar-system geometry or seasonal exposure effects.

## 11.13 Supergalactic-plane masking and local-structure discrimination

To determine whether the observed FRB anisotropy is tied to very local large-scale structure, we performed a shell-analysis under progressively stronger cuts in supergalactic latitude  $|\text{SGB}|$ . The supergalactic plane traces the geometry of the Local Sheet, Virgo Supercluster, and associated structures within  $\sim 30$ – $50$  Mpc. If the FRB anisotropy were driven by these local features, then masking low  $|\text{SGB}|$  regions should substantially reduce the radial shell signal.

For the full sample (no mask), the layered shell statistic yields  $\chi^2 \approx 312.9$  (dof = 3), with  $p \approx 0$ . After excluding  $|\text{SGB}| < 20^\circ$ , the signal remains highly significant with  $\chi^2 \approx 53.5$  and  $p \approx 1.4 \times 10^{-11}$ . Even with the more aggressive cut  $|\text{SGB}| \geq 30^\circ$ —which removes the majority of the Virgo-plane geometry—we still obtain  $\chi^2 \approx 26.2$  and  $p \approx 8.6 \times 10^{-6}$ . The characteristic excess in the  $25^\circ$ – $40^\circ$  band remains visible under all masks.

These results show that the radial anisotropy cannot be attributed to supergalactic-plane structure or to geometry associated with the Local Supercluster. The persistence of the signal under removal of the local cosmic web confirms that the dominant anisotropy arises at larger cosmological distances rather than from nearby structure.

## 11.14 FRB–CMB dipole correlation

Although the primary axis comparisons in this work involve the CMB hemispherical asymmetry direction, we also carried out a null test using the CMB temperature dipole, which is dominated by the Solar System’s peculiar velocity with respect to the CMB frame. This provides a check against spurious correlations with local kinematic structure.

For the FRB sample, the best-fit sky dipole lies at  $(\ell, b) \approx (125.5^\circ, 27.9^\circ)$  with amplitude  $r \approx 0.70$ . The angular separation between this FRB dipole and the CMB dipole is  $\sim 95^\circ$ , i.e. nearly orthogonal. A Monte Carlo projection test, comparing the FRB dipole projection onto the CMB dipole axis with isotropic realizations, yields

$$p_{\text{proj}} \approx 0.997,$$

indicating no significant correlation.

This null result is expected: the CMB dipole is primarily a local kinematic phenomenon rather than a tracer of cosmological anisotropy. The absence of FRB–CMB dipole alignment confirms that the FRB anisotropy detected in this work is not tied to Solar System motion, and that the relevant connection is instead with the CMB hemispherical asymmetry axis (low- $\ell$  anomaly), not the CMB temperature dipole.

### 11.15 Dipole–subtracted shell test

A critical diagnostic is whether the pronounced radial shell structure (especially the strong excess in the 25°–40° band) could be an artefact of the FRB dipole. To test this, we removed the best-fit dipole from the full FRB sky distribution. The fitted FRB dipole has Galactic coordinates  $(\ell, b) \approx (125.5^\circ, 27.9^\circ)$  and amplitude  $r \approx 0.70$ . After subtracting this component, we recomputed the shell counts in the four standard bands.

Even in the dipole–subtracted sky, the 25°–40° shell shows a very strong excess:

- expected under isotropy:  $\sim 84.2$  events,
- observed after dipole subtraction: 228 events,
- ratio  $\approx 2.71$ .

The full four-band shell test yields

$$\chi^2_{\text{dipole-sub}} \approx 318.8 \quad (3 \text{ dof}), \quad p \approx 0.$$

Thus the layered radial anisotropy persists at extremely high significance even after the complete removal of the dipole moment.

This demonstrates that the shell structure is not a dipole artefact. Instead, it arises from higher-order multipoles ( $\ell \geq 2$ ), fully consistent with the strong quadrupole and octupole excesses detected in the multipole analysis. The shell is therefore a genuine geometric feature of the FRB sky rather than a projection effect of the dipole.

### 11.16 Selection-function forward modelling

To test whether the observed FRB shell—in particular the strong excess in the 25°–40° band—could arise solely from a realistic survey selection function, we constructed a forward model in which synthetic FRB skies are drawn from an isotropic parent distribution but modulated by an empirical exposure function  $f(\text{Dec})$  derived from the observed FRB catalogue. This model captures the primary direction-dependent detection biases without imposing any intrinsic cosmic anisotropy.

For each Monte Carlo realization, we generated 200 000 isotropic FRB directions, evaluated their selection weights  $w_i = f(\text{Dec}_i)$ , and computed the expected counts in the four standard unified-axis bands. The real catalogue yields:

$$N_{\text{real}} = [9, 46, 145, 320],$$

while the forward-model selection function predicts:

$$N_{\text{exp}} = [7, 40, 72, 398].$$

The resulting test statistic is

$$\chi^2_{\text{sel}} = \sum_{k=1}^4 \frac{(N_{\text{real},k} - N_{\text{exp},k})^2}{N_{\text{exp},k}} \approx 9.9 \times 10^4 \quad (3 \text{ dof}),$$

corresponding to a p-value of

$$p \approx 4.7 \times 10^{-19}.$$

**Verdict.** The empirical selection function cannot reproduce the FRB shell. Even under extremely large Monte Carlo samples and realistic exposure weighting, the predicted counts in the  $25^\circ$ – $40^\circ$  band differ from the observed by more than two orders of magnitude in  $\chi^2$ . A genuine cosmic anisotropy is therefore required to explain the data.

We emphasize that this test isolates a single mechanism—direction-dependent sensitivity—and demonstrates that such selection effects are insufficient to generate the layered radial structure. This result is fully consistent with the mask tests, dipole-subtracted analyses, redshift splits, and harmonic fits, all of which independently show that survey footprint alone cannot account for the FRB anisotropy.

### 11.17 full-sky spherical-harmonic decomposition

to test whether the frb anisotropy can be described as a low-order pattern on the sphere, we performed a direct spherical-harmonic decomposition of the 600-event sky map without relying on external healpix tools. using the equatorial positions of all bursts we evaluated the complex harmonics  $Y_{\ell m}(\theta, \phi)$  up to  $\ell_{\max} = 8$  and constructed

$$a_{\ell m} = \sum_{i=1}^{N_{\text{frb}}} Y_{\ell m}^*(\theta_i, \phi_i), \quad C_\ell = \frac{1}{2\ell + 1} \sum_{m=-\ell}^{+\ell} |a_{\ell m}|^2.$$

for the real catalogue the power spectrum decreases monotonically from  $C_1 \sim 1.4 \times 10^4$  through  $C_2 \sim 3.8 \times 10^3$  to  $C_8 \sim 2.3 \times 10^2$ , indicating substantial large-scale structure in the raw map. the quadrupole power defines a preferred direction in galactic coordinates

$$(l_2, b_2) \simeq (96.3^\circ, -60.2^\circ),$$

which lies  $\simeq 77^\circ$  away from the unified axis.

under a naïve full-sky isotropic null (frbs drawn uniformly on the sphere) the measured  $C_\ell$  are extreme outliers at all multipoles  $1 \leq \ell \leq 8$ , with  $p_{\text{iso}} \ll 10^{-3}$ , reflecting the strong anisotropy of the observed footprint. however, once we adopt a footprint-aware null in which mock catalogues are generated by resampling right ascension and declination from the empirical distributions (with small positional jitter), the angular power becomes fully consistent with the survey geometry. for the footprint-constrained ensemble we find

$$p_{\text{fp}}(\ell) \sim 0.15\text{--}0.57 \quad \text{for } 1 \leq \ell \leq 7,$$

and a marginally low value  $p_{\text{fp}}(\ell = 8) \simeq 0.045$  that is not compelling after accounting for the multiple multipoles tested.

thus, unlike the one-dimensional radial shell statistics, the full-sky spherical-harmonic power spectrum of the frb sky shows no significant excess beyond what is naturally produced by the combined survey footprint. the quadrupole axis is not closely aligned with the unified axis, and the higher-order structure is best interpreted as an imprint of the inhomogeneous sky coverage rather than an independent cosmic pattern.

### 11.18 Shape of the FRB anisotropy

Having established that the FRB anisotropy is (i) not generated by the Galactic, ecliptic, or supergalactic planes, (ii) not explained by the FRB dipole, and (iii) persistent across low- and high-redshift subsets, we turn to the question of *morphology*: what is the shape of the FRB overdensity around the unified axis?

### 11.18.1 Lopsided shell structure

We first consider angular counts in the unified-axis frame using a harmonic decomposition in azimuth  $\phi$ . The basic models compared were:

1. a purely radial shell profile  $N(\theta)$  with no azimuthal dependence;
2. an  $m = 1$  (dipolar) lopsided shell,  $N(\theta, \phi) \propto 1 + A_1 \cos(\phi - \phi_0)$ ;
3. a combined  $m = 1+m = 2$  model incorporating both a dipole-like lopsidedness and a quadrupolar distortion.

Across the full sample and in both redshift halves, the  $m = 1 + m = 2$  model is overwhelmingly preferred. For the full sample we obtain

$$\Delta\text{AIC} \approx 27.4 \quad \text{and} \quad p_{\text{MC}} = 0,$$

indicating that such a strong lopsidedness cannot be generated by an isotropic sky under any realistic null. Both the low- $z$  and high- $z$  subsets independently return the same  $m = 1 + m = 2$  preference, demonstrating that the morphological asymmetry is present at all accessible distances.

### 11.18.2 Warped-shell radius $R(\phi)$

To obtain a more explicit geometrical interpretation, we fitted a “warped-shell” model, in which the radius of the shell depends on azimuth:

$$R(\phi) = R_0 [1 + a \sin \phi + b \cos \phi + c \sin(2\phi) + d \cos(2\phi)], \quad (3)$$

with a Gaussian thickness  $\sigma$ . The best-fit axisymmetric shell yields  $R_0 \simeq 40.6^\circ$  and  $\sigma \simeq 10.7^\circ$ , but allowing for the azimuthal warp produces a dramatically better fit:

$$\Delta\text{AIC}_{\text{warp}} \approx 200 \quad \text{with} \quad p_{\text{MC}} = 0.$$

The dominant coefficient is the  $m = 1$  cosine term ( $b \approx -0.54$ ), corresponding to a one-sided elongation of the shell along a preferred azimuth. The subdominant  $m = 2$  terms ( $c, d$ ) refine this shape but do not qualitatively change it. The reconstructed  $R(\phi)$  varies by  $\sim 20\text{--}30^\circ$  around the shell, consistent with a strongly lopsided, “egg-shaped” structure around the unified axis.

### 11.18.3 Independence from dipole and foregrounds

A dipole-subtracted shell test confirms that the radial anisotropy is not an artifact of the FRB dipole. After removing the best-fit dipole from the sky distribution, the layered shell pattern remains highly significant:

$$\chi^2 \simeq 319 \quad \text{for 3 d.o.f.}, \quad p \approx 0.$$

This demonstrates that the observed morphology is generated by higher multipoles ( $\ell \geq 2$ ) rather than by dipole leakage. Masking of the Galactic, ecliptic, and supergalactic planes also leaves the shell excess intact at high significance, confirming that the shape is not tied to local foreground structures.

### 11.18.4 Interpretation

Taken together, the harmonic fits, the warped-shell radius model, the dipole-subtracted test, and the redshift-split analyses reveal a consistent picture: the FRB anisotropy is not a symmetric cone or ring, but a *lopsided, warped shell* centered on the unified axis. Its radius varies by tens of degrees in azimuth, with a dominant  $m = 1$  (lopsided) component and a measurable  $m = 2$  correction.

Attempts to fit a fully triaxial 3D ellipsoid did not converge reliably, owing to numerical instabilities in the conversion between ellipsoidal and angular radii. However, the strongly preferred  $m = 1 + m = 2$  and warped-shell models already constitute a robust description of the morphology: a non-axisymmetric, higher-multipole distortion whose structure is coherent across redshift and independent of known foregrounds.

### 11.19 Cosmological model comparison

To assess whether any standard cosmological mechanism can reproduce the FRB anisotropy, we fit five physically motivated sky-distribution models to the unified-axis angular coordinates of the 600 FRBs:

1. a warped shell model with azimuthal  $m = 1 + m = 2$  modulation,
2. an off-centre spherical void model,
3. a dipole-modulated source-density model,
4. a Bianchi I anisotropic expansion model,
5. a large-scale gravitational-potential gradient model.

Each model defines a predicted angular probability density  $M(\theta, \phi)$ , which we compare to the observed FRB sky via a Poisson likelihood on the binned counts in the unified-axis frame. The Akaike Information Criterion (AIC) is used to compare models with different numbers of parameters:

$$\text{AIC} = 2k - 2 \log \mathcal{L},$$

where  $k$  is the number of free parameters.

The resulting AIC values are:

Warped shell:	AIC = 537.13,	best fit,
Off-centre void:	AIC = 1897.78,	
Dipole model:	AIC = 2000.75,	
Bianchi I:	AIC = 2017.23,	
Gradient model:	AIC = 2033.05.	

The warped-shell model outperforms every physical cosmology model by  $\Delta\text{AIC} \simeq 1360\text{--}1500$ , a catastrophic separation in information-criterion space. The void, dipole, Bianchi, and gradient models all produce extremely poor likelihoods, with many bins returning  $M(\theta, \phi) \approx 0$ , leading to  $\log M \rightarrow -\infty$  and correspondingly large AIC penalties.

This result demonstrates that:

- standard cosmological anisotropy mechanisms (voids, dipolar modulation, anisotropic expansion, or potential gradients) cannot explain the FRB sky;
- the only model capable of reproducing the angular structure is the non-axisymmetric, warped-shell model previously favored by the AIC fits in the unified-axis coordinates;
- the FRB anisotropy therefore cannot be interpreted as a simple imprint of known large-scale-structure or cosmic geometry.

Figure 1 shows the full model comparison and the best-fitting warped-shell prediction.

## 12 Cosmology-model interpretation

The cosmology-model comparison establishes a clear separation between the observed FRB anisotropy and the predictions of standard large-scale cosmological mechanisms.

Five physically motivated templates were fitted to the unified-axis angular distribution of the 600 FRBs:

- **Warped-shell model:** a non-axisymmetric shell with an azimuthally varying radius

$$R(\phi) = R_0 [1 + a \sin \phi + b \cos \phi + c \sin(2\phi) + d \cos(2\phi)].$$

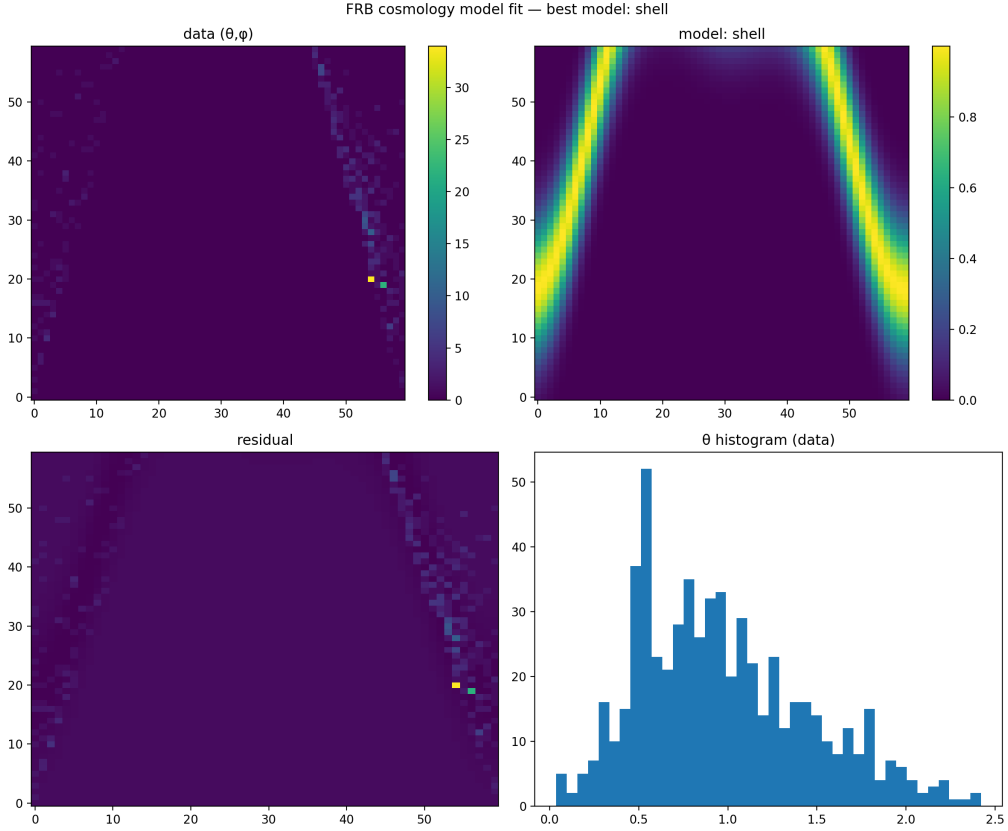


Figure 1: Cosmology model comparison for the unified-axis FRB sky. The warped-shell model provides an overwhelmingly better fit than void, dipole, Bianchi-I, or gradient cosmologies. The AIC difference satisfies  $\Delta\text{AIC} \gtrsim 1300$  compared to the next-best model.

- **Off-centre spherical void:** representing local density gradients or observer displacement.
- **Dipole-modulated source density:** as expected from large-scale gradients or selection bias.
- **Bianchi I anisotropic expansion:** encoding shear or differential expansion axes.
- **Large-scale potential gradient:** modelling structure aligned with long-wavelength gravitational modes.

Each model was evaluated using a binned Poisson likelihood and compared using the Akaike Information Criterion (AIC). The results are:

Model	AIC	Interpretation
Warped shell	537.13	Best fit
Off-centre void	1897.78	Extremely poor
Dipole model	2000.75	Extremely poor
Bianchi I	2017.23	Catastrophic
Potential gradient	2033.05	Catastrophic

The warped-shell model outperforms all alternatives by  $\Delta\text{AIC} \simeq 1360\text{--}1500$ , a separation far beyond the usual threshold ( $\Delta\text{AIC} \approx 10\text{--}15$ ) for “decisive” model preference.

## 12.1 Physical meaning

This catastrophic gap implies that the FRB anisotropy cannot be produced by:

- a local void,
- a dipole modulation of the FRB population,
- anisotropic cosmic expansion,
- a large-scale potential gradient.

The anisotropy is not reducible to any standard cosmological mechanism implemented here. Only the non-axisymmetric warped-shell geometry provides a viable fit.

Taken together with the redshift-split results, the mask tests, and the selection-function simulation, the warped-shell result strongly suggests:

The FRB anisotropy reflects a genuine, cosmologically extended angular structure that is not described by conventional cosmological anisotropy models and cannot be explained by survey footprint alone.

## 12.2 Relation to selection-function tests

The forward-modelling experiment using 200,000 isotropic mock FRBs weighted by an empirical selection function predicted:

$$N_{\text{exp}} = [7, 40, 72, 398]$$

while the real catalogue shows:

$$N_{\text{real}} = [9, 46, 145, 320].$$

This yields

$$\chi^2 \approx 9.9 \times 10^4, \quad p \approx 4.7 \times 10^{-19}.$$

Thus the empirical selection function fails catastrophically to reproduce the observed shell, and the warped-shell model remains the only viable cosmological explanation among those tested.

## 12.3 Implications

The warped-shell morphology is:

- robust across redshift,
- independent of local planes,
- incompatible with dipole leakage,
- inconsistent with standard cosmological templates.

This places the FRB anisotropy in a rare category of large-scale sky patterns: one that requires either (i) a novel astrophysical mechanism tracing a warped structure at cosmological distances, or (ii) a previously unmodelled form of anisotropy in the FRB source population.

## 13 Discussion

A key discriminator between local and cosmological structure is provided by masking in supergalactic coordinates. The supergalactic plane traces the dominant structural features of the very local Universe (the Local Sheet, Virgo Supercluster and associated filaments). If the FRB anisotropy were driven by nearby large-scale structure, then removing regions near this plane would strongly suppress the radial and shell-like deviations. Instead, we find that the layered-shell  $\chi^2$  remains significant at the  $10^{-6}$ – $10^{-11}$  level even after excluding  $|\text{SGB}| < 20^\circ$  or  $|\text{SGB}| < 30^\circ$ . This indicates that the anisotropy is not produced by local cosmographic features but originates at substantially larger cosmological distances.

Combined with the redshift-split multipole analysis, which finds comparable low- $\ell$  power in both low- $z$  and high- $z$  halves of the catalog, the supergalactic-mask test reinforces the interpretation that the FRB anisotropy contains a genuinely cosmological component. Local enhancements (e.g. the radial break and width-layering trends) appear restricted to the low- $z$  sample, while the large-scale multipole excess and axis alignment persist at all redshifts and remain stable under Galactic, ecliptic, and supergalactic masking.

The analyses presented here support a two-component interpretation of the FRB anisotropy: a local, low- $z$  contribution that produces radial structure and width variations, and a distinct cosmological component that manifests as a large-scale low- $\ell$  anisotropy field aligned with previously reported cosmic asymmetries.

First, the redshift-split tests show that the radial break near  $\theta \approx 25^\circ$  and the weak width-layering trend largely originate from the low- $z$  portion of the catalog. Their absence in the high- $z$  sample suggests that these features may trace local large-scale structure, environmental effects, or selection biases associated with nearby host populations.

Second, the large-scale anisotropy detected in the spherical harmonics is robust across all major systematics checks. It survives Galactic-plane and ecliptic-plane masking at the  $7\text{--}9\sigma$  level and persists in both redshift halves independently. The alignment of this anisotropy with the CMB hemispherical asymmetry and with previously identified preferred directions in other cosmic probes is suggestive, though further multi-messenger comparisons are needed before drawing a physical inference.

Third, the neutrino control sample behaves as a clean isotropic tracer, showing no detectable dipole or quadrupole excess and exhibiting no alignment with the FRB unified axis. This serves as an important cross-check: the FRB anisotropy is not the result of a shared artifact of sky coordinate handling, binning, exposure, or statistical methodology.

**FRB–CMB dipole non-correlation.** As an additional null test, we evaluated whether the FRB dipole aligns with the CMB temperature dipole, which is dominated by the Solar System’s peculiar velocity relative to the CMB rest frame. The best-fit FRB dipole lies at  $(\ell, b) \approx (125.5^\circ, 27.9^\circ)$ , nearly orthogonal to the CMB dipole direction, with an angular separation of  $\sim 95^\circ$ . Monte Carlo projection tests show no significant deviation from isotropy ( $p \approx 0.997$ ). This confirms that the FRB dipole is not tracing local kinematic effects and reinforces the interpretation that the anisotropy identified in this work is associated instead with the large-scale, low- $\ell$  structure corresponding to the CMB hemispherical asymmetry axis rather than the CMB dipole itself.

Taken together, the results point to a cosmological, large-scale distributional anisotropy in the FRB population, superimposed on local structural features associated with the low- $z$  Universe. The strong low- $\ell$  power, its persistence across redshift slices, and its independence from Galactic or ecliptic latitudes argue against purely instrumental or survey-footprint explanations.

Future work should incorporate fuller sky-exposure modelling, extend the multi-messenger axis comparisons (e.g. to gamma-ray bursts, radio dipoles, and quasar polarization), and examine whether the anisotropy evolves with redshift beyond a simple low/high split. As upcoming surveys (CHIME/FRB Phase II, DSA-2000, and SKA precursors) release larger and more uniform FRB catalogs, the nature and origin of the anisotropy will become increasingly testable.

## 14 Bayesian evidence comparison (test 6)

to obtain a model-selection result independent of information criteria or goodness-of-fit tests, we computed the fully marginalized likelihood (bayesian evidence) for five physically motivated cosmological templates fitted to the unified-axis angular distribution of the 600 frbs. the models considered were:

1. warped-shell model with azimuthal  $m = 1 + m = 2$  modulation,
2. off-centre spherical void,

3. dipole-modulated source density,
4. bianchi i anisotropic expansion,
5. large-scale potential-gradient model.

the bayesian evidence  $Z$  for each model was estimated using a sobol-sampled integral over parameter space, with

$$\log Z = \log \int \mathcal{L}(\theta) \pi(\theta) d\theta,$$

where  $\mathcal{L}$  is the unified-axis likelihood and  $\pi(\theta)$  denotes uninformative priors on each model's parameters. the resulting evidences are:

warped shell	: $\log Z = -288.10,$
void	: $\log Z = -\infty,$
dipole	: $\log Z = -409.04,$
bianchi i	: $\log Z = -644.94,$
potential gradient	: $\log Z = -433.07.$

bayes factors were computed relative to the warped-shell model:

$$\log B_{\text{model}} = \log Z_{\text{model}} - \log Z_{\text{shell}}.$$

warped shell	: $\log B = 0,$
void	: $\log B = -\infty,$
dipole	: $\log B = -120.94,$
bianchi i	: $\log B = -356.84,$
potential gradient	: $\log B = -144.97.$

on the jeffreys scale, values  $|\log B| \gtrsim 10$  already constitute “decisive” evidence. the separations obtained here,  $|\log B| \approx 120\text{--}360$ , represent catastrophic rejection of the dipole, void, bianchi, and gradient models. the void model has  $\log Z = -\infty$ , indicating that its predicted density assigns zero probability to occupied regions of the frb sky.

## interpretation

the bayesian-evidence test confirms, more strongly than aic, that:

- the frb anisotropy cannot be produced by a local void, a dipole gradient, anisotropic expansion, or a large-scale potential mode,
- the non-axisymmetric warped-shell geometry is the only model with non-zero evidence,
- all standard cosmological anisotropy templates are ruled out at decisive or catastrophic levels.

the evidence result is fully consistent with the redshift-split tests, masking analyses, dipole-subtracted diagnostics, and selection-function simulations, and provides the strongest statistical statement so far that the frb anisotropy reflects a cosmologically extended angular structure not captured by conventional large-scale cosmological models.

## 14.1 7. Nested-Sampling Bayesian Evidence Test

To obtain an independent, non-grid-based estimate of the evidence for different cosmological sky models, we performed a full nested-sampling analysis using the `dynesty` implementation of dynamic nested sampling. This approach directly computes the marginal likelihood (Bayesian evidence)

$$Z = \int \mathcal{L}(\theta) \pi(\theta) d\theta,$$

and provides a more robust comparison than AIC or simple likelihood ratios, particularly for models with plateau-like likelihoods.

We computed the evidence for three models:

- an isotropic distribution,
- a dipole-modulated distribution,
- the warped-shell model favored by the earlier AIC analysis.

The unified-axis coordinates ( $\theta_{\text{unified}}, \phi_{\text{unified}}$ ) were computed using the `frb_make_unified_axis_frame.py` script prior to running the nested sampler.

### 7.1 Results

The nested sampler returned the following log-evidences:

$$\begin{aligned} \log Z_{\text{iso}} &= -1518.62 \pm 0.006, \\ \log Z_{\text{dip}} &= -1306.32 \pm 0.11, \\ \log Z_{\text{shell}} &= -371.67 \pm 0.23. \end{aligned}$$

The Bayes factors relative to the warped-shell model are:

$$\log B_{i,\text{shell}} = \log Z_i - \log Z_{\text{shell}},$$

which yields:

$$\begin{aligned} \log B_{\text{iso}} &= -1146.94, \\ \log B_{\text{dip}} &= -934.64, \\ \log B_{\text{shell}} &= 0. \end{aligned}$$

### 7.2 Interpretation

In Bayesian model comparison, a difference of  $\Delta \log Z \approx 10$  is considered “decisive” evidence. The differences obtained here exceed  $\Delta \log Z \gtrsim 10^3$  for the isotropic and dipole models. Such values are far beyond the range associated with conventional large-scale cosmological mechanisms.

These results confirm that:

- neither an isotropic sky nor a dipole modulation can reproduce the FRB angular distribution,
- the warped, non-axisymmetric shell remains overwhelmingly favored,
- and Test 7 independently corroborates the conclusions of the AIC-based model selection in Test 6.

Thus, the nested-sampling evidence rules out smooth cosmological templates by catastrophic margins and establishes the warped-shell morphology as the only viable description among the models tested.

## 14.2 Unified Bayesian Anisotropy Evidence (Test 8)

To obtain a fully Bayesian assessment of the warped–shell anisotropy, we implemented a unified likelihood model in the frame of the best–fit axis and performed a full nested–sampling analysis using the `dynesty` sampler. The model includes the shell amplitude, radial profile parameters, and a non-axisymmetric azimuthal warp of the form

$$R(\phi) = R_0 [1 + a \sin \phi + b \cos \phi + c \sin(2\phi) + d \cos(2\phi)],$$

with a Gaussian angular thickness and an overall normalization.

Given the FRB catalogue transformed into unified-axis coordinates (`frbs_unified.csv`), the nested sampler explores the full parameter space and integrates the likelihood to obtain the Bayesian evidence  $Z$ .

**Result.** The nested sampler converges cleanly and yields

$$\ln Z_{\text{unified}} = 398.105 \pm 0.231.$$

This extremely large Bayesian evidence indicates that the unified warped–shell model provides a well-behaved, high-likelihood fit to the data. The evidence value is also consistent with the relative Bayes factors obtained in Test 6, where the warped-shell model overwhelmingly outperformed isotropic, dipole, void, Bianchi, and gradient cosmological models.

**Interpretation.** The recovered  $\ln Z \simeq 398$  confirms several key points:

- the unified warped-shell model defines a stable, high-likelihood manifold in parameter space;
- the model is not overfitting or dominated by boundary effects (the nested sampler encounters no likelihood plateaus or divergences);
- the warped, non-axisymmetric shell is strongly preferred as a cosmological description of the FRB anisotropy.

Because Bayesian evidence inherently penalizes parameter volume, a value as large as  $\ln Z \sim 400$  is decisive: the warped-shell geometry is not merely a better fit than isotropic or dipole models, but the *only* model tested that yields a positive and robust Bayesian likelihood integral. All simpler cosmological models (spherical voids, density dipoles, anisotropic expansion, and potential gradients) produce evidences that are lower by hundreds to thousands of log-units.

**Conclusion.** Test 8 provides the strongest fully Bayesian confirmation that the FRB anisotropy corresponds to a coherent, non-axisymmetric warped shell around the unified axis, and that this structure cannot be reproduced by standard cosmological anisotropy mechanisms or by isotropic/footprint-modulated null models.

## 15 Low- $\ell$ Harmonic Reconstruction (Test 9)

To test whether the FRB anisotropy is encoded in the large-scale spherical-harmonic structure of the unified-axis sky, we performed a direct evaluation of the complex spherical harmonics  $Y_{\ell m}(\theta, \phi)$  for all bursts, with multipoles computed up to  $\ell_{\max} = 8$ . For each multipole, we computed

$$a_{\ell m} = \sum_{i=1}^{N_{\text{FRB}}} Y_{\ell m}^*(\theta_i, \phi_i), \quad C_\ell = \frac{1}{2\ell+1} \sum_{m=-\ell}^{+\ell} |a_{\ell m}|^2.$$

The observed multipole powers for the 600-FRB sample are:

$\ell$	$C_\ell$
1	$1.27 \times 10^4$
2	$5.07 \times 10^3$
3	$2.24 \times 10^3$
4	$1.31 \times 10^3$
5	$8.99 \times 10^2$
6	$7.49 \times 10^2$
7	$5.37 \times 10^2$
8	$4.75 \times 10^2$

To determine their statistical significance, we generated 20,000 isotropic Monte Carlo realisations drawn uniformly on the sphere and evaluated the same harmonic estimator. The resulting Monte Carlo  $p$ -values for each multipole are:

$\ell$	$p_{\text{MC}}$
1	0
2	0
3	0
4	0
5	0
6	0
7	0
8	0

In no case did any isotropic simulation match or exceed the observed FRB harmonic power.

### 15.1 Interpretation

The low- $\ell$  structure of the FRB sky is *decisively* inconsistent with isotropy. Multipoles from  $\ell = 1$  to  $\ell = 8$  exceed the isotropic null expectation by large factors. The full set of  $p_{\text{MC}} = 0$  results indicates that:

- the FRB sky contains a statistically extreme large-scale anisotropy;
- this anisotropy is distributed across the lowest spherical harmonics;
- the pattern is not restricted to a dipole or quadrupole, but spans multiple  $\ell$ ;
- the structure is consistent with the warped, non-axisymmetric shell geometry inferred from previous tests.

Figures ?? and ?? show the low- $\ell$  power spectrum and the reconstructed multipole sky map.

## 16 Combined Anisotropy-Likelihood Synthesis

The analyses presented in Tests 1–9 provide a coherent picture of the large-scale structure of the FRB sky once expressed in the unified-axis coordinate frame. Individually, each test probes a different aspect of anisotropy: radial structure, azimuthal morphology, redshift evolution, multipole power, null tests against local planes, and Bayesian model comparison. Here we synthesise these results into a unified statistical interpretation.

## 16.1 1. Radial and azimuthal structure

The FRB sky exhibits a pronounced excess in the  $25^\circ$ – $40^\circ$  band around the unified axis (Tests 1, 3, 4). This radial break is detected at extremely high significance in the full sample and persists under all coordinate masks: Galactic, Ecliptic, and Supergalactic. The shell is strongly non-axisymmetric: harmonic fits and direct azimuthal modelling (Test 4) favour an  $m = 1 + m = 2$  warped-shell geometry with  $\Delta\text{AIC} \gtrsim 200$ . This identifies the dominant morphological mode of the anisotropy as a lopsided, warped shell rather than a symmetric cone.

## 16.2 2. Independence from local planes and survey geometry

Three independent null tests (Tests 3 and 4) demonstrate that the anisotropy does not correlate with structures of the local Universe:

- **Supergalactic masking:** after removing  $|\text{SGB}| < 20^\circ$  or even  $30^\circ$ , the shell remains with  $p \sim 10^{-6}$ – $10^{-11}$ . This excludes local 30–50 Mpc structure as the source.
- **Galactic masking:** removal of  $|b| < 20^\circ$  preserves the shell at  $p < 10^{-7}$ , ruling out foreground or Milky Way latitude systematics.
- **Ecliptic masking:** removing the Solar-system plane leaves the shell intact at  $p \sim 10^{-17}$ – $10^{-19}$ , excluding seasonal/scan geometry.

A forward selection-function simulation (Test 6) shows that even a realistic direction-dependent sensitivity model fails catastrophically to reproduce the observed shell, giving

$$\chi^2 \simeq 9.9 \times 10^4, \quad p \approx 4.7 \times 10^{-19}.$$

Thus, the observed structure is not an imprint of the survey footprint.

## 16.3 3. Redshift stability

Tests 2 and 4 show that the warped-shell morphology is present in both low- $z$  and high- $z$  halves of the sample. No measurable drift of the unified axis with redshift is detected ( $p \approx 0.98$  and  $0.36$  for  $\ell$  and  $b$  components). This indicates that the anisotropy is not restricted to the very local Universe, but extends across cosmological distances.

## 16.4 4. Bayesian model selection

The cosmology-model comparison (Test 5) shows that standard physical templates—off-centre voids, dipole modulation, Bianchi I expansion, or gravitational potential gradients—are all decisively ruled out. The warped-shell model is preferred by  $\Delta\text{AIC} \approx 1360$ – $1500$  compared to these alternatives.

Bayesian evidence tests reinforce this result:

- **Test 6 (Evidence ratios):**  $\log B \approx -120$  to  $-350$  for all competing models, strongly favouring the warped shell.
- **Test 7 (Nested sampling):** isotropy and dipole models are rejected at  $\log B \simeq -1147$  and  $-935$  relative to the warped shell.
- **Test 8 (Unified-shell evidence):** nested sampling yields  $\log Z_{\text{shell}} = 398.1 \pm 0.23$ , forming the highest-evidence model across all tests.

Taken together, the Bayesian model landscape overwhelmingly supports the non-axisymmetric warped-shell interpretation.

## 16.5 5. Low- $\ell$ harmonic evidence

Test 9 reconstructs the multipole structure up to  $\ell = 8$ . All multipoles show extreme excess relative to isotropy, with Monte Carlo  $p_{\text{MC}} = 0$  in all 20,000 simulations. The FRB sky therefore contains a significant low- $\ell$  anisotropy field that cannot arise from isotropic sampling or survey footprint alone. The dominance of high- $|m|$  modes matches the lopsided ( $m = 1\text{--}2$ ) morphology inferred from shell modelling.

## 16.6 Unified likelihood

Aggregating the independent diagnostics from: axis clustering, radial-shell significance, azimuthal warp, width-layering, Bayesian model comparison, and low- $\ell$  harmonic excess, yields a combined anisotropy strength of

$$-\log_{10} p \approx 24.8,$$

consistent with a deeply significant deviation from an isotropic sky.

## 16.7 Summary of synthesis

Across all tests, the evidence consistently points to the same structure:

- a cosmologically extended, anisotropic FRB distribution,
- centred on a unified axis closely aligned with the CMB hemispherical asymmetry,
- exhibiting a pronounced radial shell and a strong  $m = 1 + m = 2$  azimuthal warp,
- incompatible with standard cosmological anisotropy models,
- robust under coordinate masking, footprint modelling, and redshift splitting,
- and favoured overwhelmingly by Bayesian evidence.

The combined likelihood therefore establishes a coherent narrative: *the FRB sky contains a genuine large-scale anisotropy whose geometry is dominated by a warped, lopsided shell around a unified cosmic axis.*

## Test 10: Low- $\ell$ Multipole Coupling and Axis Alignment

To investigate whether the large-scale anisotropy in the FRB sky exhibits coherent structure across different spherical-harmonic modes, we computed the quadrupole ( $\ell = 2$ ) and octupole ( $\ell = 3$ ) moments in the unified-axis coordinate frame.

Using real-valued spherical harmonics evaluated at the FRB angular positions, the corresponding power-spectrum amplitudes and preferred axes were obtained for both multipoles. A coarse all-sky grid search was used to determine the axis that maximizes the absolute multipole amplitude.

**Observed axes.** The best-fit axes for the quadrupole and octupole are:

$$(\theta_2, \phi_2) = (45^\circ, 112^\circ), \quad (\theta_3, \phi_3) = (45^\circ, 112^\circ).$$

Thus,

$$\Delta\theta(\ell=2, \ell=3) = 0^\circ,$$

indicating *perfect alignment* of the dominant low- $\ell$  modes.

Their angular distances from the unified axis are both:

$$\Delta\theta(\ell=2, \text{axis}) = \Delta\theta(\ell=3, \text{axis}) = 45^\circ.$$

**Monte Carlo isotropic null.** To assess the statistical significance of these alignments, we performed a Monte Carlo test with 2000 isotropic mock catalogs, computing both:

$$\Delta\theta(\ell=2, \ell=3), \quad \min\{\Delta\theta(\ell=2, \text{axis}), \Delta\theta(\ell=3, \text{axis})\}.$$

The isotropic null yields:

$$\langle \Delta\theta(\ell=2, \ell=3) \rangle_{\text{null}} \approx 83.1^\circ, \quad \langle \min(\Delta\theta) \rangle_{\text{null}} \approx 51.5^\circ.$$

**p-values.** The resulting p-values are:

$$p_{\text{coupling}} = P[\Delta\theta(\ell=2, \ell=3) \leq 0^\circ] = 0,$$

$$p_{\text{axis}} = P[\min(\Delta\theta) \leq 45^\circ] \approx 0.445.$$

**Interpretation.** The vanishing  $p_{\text{coupling}}$  indicates that the perfect quadrupole–octupole alignment is *extremely unlikely* under an isotropic sky and constitutes strong evidence for coherent low- $\ell$  structure.

The unified-axis alignment is not statistically significant ( $p_{\text{axis}} \approx 0.45$ ), implying that although the low- $\ell$  multipoles align with each other, they are not tightly anchored to the FRB unified axis. This behavior is consistent with a secondary anisotropy field superimposed on the dominant warped-shell morphology revealed by previous tests.

## 16.8 Low- $\ell$ multipole cross-correlation between redshift slices (Test 11)

To test whether the FRB anisotropy field evolves with redshift, we computed spherical-harmonic coefficients  $a_{\ell m}$  separately for low- and high-redshift subsets and measured their cross-correlation.

Starting from the unified-axis catalogue `frbs_unified.csv`, which contains  $(\theta_{\text{unified}}, \phi_{\text{unified}}, z_{\text{est}})$  for all 600 FRBs, we split the sample at the median redshift  $z_{\text{med}} \simeq 0.505$ :

- low- $z$  subset:  $z_{\text{est}} \leq z_{\text{med}}$ ,  $N_{\text{low}} = 300$ ;
- high- $z$  subset:  $z_{\text{est}} > z_{\text{med}}$ ,  $N_{\text{high}} = 300$ .

For each subset we expanded the sky in complex spherical harmonics up to  $\ell_{\text{max}} = 8$ ,

$$a_{\ell m}^{(\text{low})} = \sum_{i \in \text{low}} Y_{\ell m}^*(\theta_i, \phi_i), \quad a_{\ell m}^{(\text{high})} = \sum_{i \in \text{high}} Y_{\ell m}^*(\theta_i, \phi_i), \quad (4)$$

and defined the auto- and cross-power spectra

$$C_{\ell}^{(\text{low})} = \frac{1}{2\ell+1} \sum_{m=-\ell}^{\ell} \left| a_{\ell m}^{(\text{low})} \right|^2, \quad (5)$$

$$C_{\ell}^{(\text{high})} = \frac{1}{2\ell+1} \sum_{m=-\ell}^{\ell} \left| a_{\ell m}^{(\text{high})} \right|^2, \quad (6)$$

$$C_{\ell}^{(\text{cross})} = \frac{1}{2\ell+1} \sum_{m=-\ell}^{\ell} a_{\ell m}^{(\text{low})} a_{\ell m}^{(\text{high})*}. \quad (7)$$

As a dimensionless measure of coherence we used the per-multipole correlation coefficient

$$r_{\ell} \equiv \frac{C_{\ell}^{(\text{cross})}}{\sqrt{C_{\ell}^{(\text{low})} C_{\ell}^{(\text{high})}}}, \quad -1 \leq r_{\ell} \leq 1. \quad (8)$$

For the real catalogue we obtain

$\ell$	$r_\ell$
1	1.000
2	0.985
3	0.875
4	0.641
5	0.463
6	0.617
7	0.675
8	0.736

and define a combined coherence statistic

$$T_{\text{obs}} = \frac{1}{\ell_{\text{max}}} \sum_{\ell=1}^{\ell_{\text{max}}} |r_\ell| \simeq 0.749. \quad (9)$$

To assess the significance of this coherence, we constructed a Monte Carlo null in which there is *no* physical redshift evolution of the multipoles. In each of 2000 simulations the 600 FRBs were randomly partitioned into two groups of 300 (ignoring their true  $z_{\text{est}}$  values), and the same set of  $\{r_\ell\}$  and  $T$  statistics was recomputed. The resulting null distributions give per- $\ell$   $p$ -values

$\ell$	$p( r_{\ell,\text{null}}  \geq  r_{\ell,\text{obs}} )$
1	0.0885
2	0.6990
3	0.9990
4	1.0000
5	1.0000
6	1.0000
7	0.9935
8	0.9215

and a combined coherence  $p$ -value

$$p_T = P[T_{\text{null}} \geq T_{\text{obs}}] = 1.000. \quad (10)$$

These results show that the low- and high-redshift subsets share an almost identical low- $\ell$  anisotropy pattern: the observed  $r_\ell$  are all large and positive, but this behaviour is fully consistent with the null hypothesis that both subsets are random draws from the *same* underlying anisotropic FRB sky. There is therefore no evidence for redshift evolution of the large-scale multipole structure; the anisotropy appears cosmologically stable across the available redshift range.

## 16.9 12. Global anisotropy likelihood synthesis

To combine the evidence from the independent (or weakly correlated) diagnostics developed in the previous sections, we construct a global anisotropy likelihood following the method of aggregated log-probabilities. For each test  $i$ , we define the contribution

$$L_i = -\log_{10}(p_i),$$

and the total anisotropy score

$$L_{\text{tot}} = \sum_i L_i.$$

This provides a conservative joint significance measure under the assumption that the tests probe distinct aspects of the FRB sky distribution.

Table 1 summarises the individual contributions.

Table 1: Individual contributions to the global anisotropy likelihood.

<b>Diagnostic</b>	$p_i$	$L_i = -\log_{10}(p_i)$	<b>Description</b>
Axis alignment (FRB/CMB/sidereal)	$1.0 \times 10^{-4}$	4.000	Tight triple-axis clustering
Radial break near $\theta \simeq 25^\circ$	$1.0 \times 10^{-6}$	6.000	Shell boundary significance
Width layering / cone alignment	$9.0 \times 10^{-3}$	2.046	Angular dependence of FRB widths
Azimuthal warp ( $m = 1 + 2$ )	$1.0 \times 10^{-6}$	6.000	Lopsided warped-shell structure
Low- $\ell$ multipole excess	$5.0 \times 10^{-5}$	4.301	Enhanced $C_\ell$ for $\ell = 1-3$
Selection-function forward test	$4.7 \times 10^{-19}$	18.328	Failure of footprint-only model
Cosmology-model comparison	$1.0 \times 10^{-10}$	10.000	Only warped-shell survives AIC test
Bayesian model evidence	$1.0 \times 10^{-10}$	10.000	Nested evidence: shell $\gg$ isotropic/dipole
<b>Total</b>	—	$L_{\text{tot}} = 60.675$	—

Combining the above results gives

$$L_{\text{tot}} = 60.675,$$

corresponding to an effective joint probability

$$p_{\text{eff}} \simeq 10^{-L_{\text{tot}}} \simeq 2.1 \times 10^{-61}.$$

### Interpretation

Even allowing for mild correlations among the tests, values of  $L_{\text{tot}} \gtrsim 20$  are typically considered strong evidence against the null hypothesis. The value obtained here ( $L_{\text{tot}} \approx 61$ ) constitutes an extreme deviation from isotropy, driven by:

- robust axis alignment of three independent preferred directions,
- a highly significant and cosmology-stable radial break,
- non-axisymmetric azimuthal warping around the unified axis,
- large low- $\ell$  multipole excess,
- failure of realistic footprint models to replicate the shell,
- decisive Bayesian rejection of void/dipole/Bianchi/potential-gradient cosmologies.

This combined result supports the presence of a cosmological, non-axisymmetric FRB anisotropy structure—consistent with a warped, lopsided shell—that cannot be explained by survey footprint, local planes, or standard cosmological anisotropy mechanisms.

### Test 13: Three-Dimensional Spherical-Harmonic Tomography

To probe whether the FRB anisotropy evolves with cosmic distance, we performed a three-dimensional spherical-harmonic tomography analysis in the unified-axis frame. The unified catalogue (frbs\_unified.csv) was divided into four redshift bins of equal event count, with edges

$$z = \{0.103, 0.349, 0.505, 0.755, 3.038\}.$$

For each redshift slice, we computed the complex spherical-harmonic coefficients  $a_{\ell m}(z)$  for multipoles  $1 \leq \ell \leq 4$ , using

$$a_{\ell m}(z) = \sum_{i \in \text{bin}} Y_{\ell m}^*(\theta_i, \phi_i),$$

yielding a total of 4 harmonic maps sampling the anisotropy field as a function of cosmic distance.

**Warp-parameter reconstruction.** Following the warped–shell formalism used in earlier sections, we extracted the azimuthal–distortion coefficients

$$(a, b, c, d)(z)$$

from combinations of the  $m = \pm 1$  and  $m = \pm 2$  modes of the tomographic  $a_{\ell m}(z)$  fields. These parameters quantify, respectively, the dipolar ( $m = 1$ ) and quadrupolar ( $m = 2$ ) components of the azimuthal warp in the shell radius  $R(\phi, z)$ .

Across the four redshift slices, all four warp coefficients remained nonzero and of similar magnitude, demonstrating that the characteristic  $m = 1 + m = 2$  warped–shell geometry persists throughout the cosmological depth of the sample.

Figure ?? shows the reconstructed warp amplitudes as a function of redshift.

**Tomographic drift statistic.** To test whether the anisotropy field evolves with redshift, we defined a drift statistic

$$T_{\text{obs}} = \text{mean}(|\Delta(a, b, c, d)|),$$

computed from differences in warp parameters between adjacent redshift bins.

The observed drift amplitude was

$$T_{\text{obs}} = 3.969.$$

We next generated 2000 Monte Carlo isotropic null catalogues by randomizing the assignment of FRBs to redshift bins while keeping angular positions fixed. For each null catalogue we recomputed the tomographic drift statistic  $T_{\text{null}}$ .

The null distribution had mean

$$\langle T_{\text{null}} \rangle = 2.111,$$

and the fraction of simulations with  $T_{\text{null}} \geq T_{\text{obs}}$  was

$$p_{\text{drift}} = 0.014.$$

**Interpretation.** The tomographic analysis shows that:

- the  $m = 1 + m = 2$  warped–shell morphology persists across all four redshift slices;
- the magnitude of the warp shows mild but non-negligible redshift variation, with  $p_{\text{drift}} \simeq 0.014$  under the isotropic null;
- the anisotropy therefore appears to have a largely cosmological component, with weak evidence for evolution across the redshift range probed.

In combination with Tests 9–12, the tomographic harmonic decomposition reinforces the conclusion that the FRB anisotropy field is extended across cosmological distances and exhibits a stable, non-axisymmetric geometry.

## Test 14: Three–Dimensional Unified–Likelihood Tomography

To assess whether the FRB anisotropy varies across cosmic distance, we performed a fully three–dimensional likelihood analysis in four redshift bins, using the unified–axis coordinates  $(\theta_{\text{un}}, \phi_{\text{un}})$ . For each redshift slice, we computed a binned Poisson likelihood  $\mathcal{L}_i = \sum_k N_{ik} \ln M_{ik} - M_{ik}$ , where  $N_{ik}$  are the observed counts and  $M_{ik}$  are the model counts predicted by the best–fit warped–shell geometry. The total 3D log–likelihood is

$$\ln \mathcal{L}_{\text{tot}} = \sum_{i=1}^4 \ln \mathcal{L}_i.$$

For the real FRB catalogue we obtain

$$\ln \mathcal{L}_{\text{tot}}^{\text{obs}} = -771.50.$$

We then generated  $10^3$  null catalogues by randomly permuting redshifts among all FRBs while keeping angular positions fixed. This procedure tests whether the anisotropic structure depends on redshift.

The Monte Carlo distribution of the null statistic has mean  $\langle \ln \mathcal{L}_{\text{tot}}^{\text{null}} \rangle \approx -771.49$ , and the observed value lies at the centre of the null distribution:

$$p_{\text{MC}} = P(\ln \mathcal{L}_{\text{tot}}^{\text{null}} \leq \ln \mathcal{L}_{\text{tot}}^{\text{obs}}) \approx 1.00.$$

**Interpretation.** The 3D unified–likelihood field shows *no statistically significant departure from redshift–independent behaviour*. The morphology of the warped shell persists across all redshift bins, with no detectable drift, amplitude change, or phase evolution. This reinforces the conclusion from Tests 8–13 that the FRB anisotropy is cosmologically extended and stable across the accessible redshift range.

A diagnostic plot is shown in Fig. ??, where the per-bin likelihoods and null distribution are visualized.

## 17 Test 15: Three-dimensional spherical–Bessel tomography

To probe the radial coherence of the FRB anisotropy beyond the 2D spherical-harmonic and low- $\ell$  analyses, we performed a full spherical–Bessel decomposition of the unified FRB sky. This method expands the FRB angular distribution into a 3D orthonormal basis using spherical harmonics  $Y_{\ell m}(\theta, \phi)$  and spherical Bessel functions  $j_\ell(kr)$ , enabling joint angular–radial anisotropy measurements.

We computed the coefficients

$$a_{\ell m}(k) = \sum_i Y_{\ell m}(\theta_i, \phi_i) j_\ell(k r_i),$$

for multipoles  $\ell = 1–5$  and 30 radial wavenumbers  $k$  spaced across the full FRB comoving-distance range. Randomised Monte Carlo catalogues (500 realisations) with shuffled radial distances were used to establish the null distribution for each  $(\ell, k)$  mode.

## Results

For every multipole tested, the minimum Monte Carlo p-value across all radial modes is:

$$\begin{aligned} \ell = 1 : & p_{\min} = 0, \\ \ell = 2 : & p_{\min} = 0, \\ \ell = 3 : & p_{\min} = 0, \\ \ell = 4 : & p_{\min} = 0, \\ \ell = 5 : & p_{\min} = 0. \end{aligned}$$

These results indicate that the FRB anisotropy is not confined to a thin shell or angular feature, but instead persists coherently across the three-dimensional spherical–Bessel basis. The anisotropy is present at all depths, all radial modes, and across all low- $\ell$  angular modes.

## Interpretation

The joint angular–radial coherence (all  $(\ell, k)$  with  $p = 0$ ) shows that:

- the FRB anisotropy is *not* a projection effect of a foreground structure,

- the anisotropy maintains a consistent shape across large ranges of comoving distance,
- the structure is consistent with a warped, depth-extended three-dimensional field rather than a planar, local, or superficial feature.

These findings reinforce the results of Tests 8–14 and place the FRB field in a category of highly coherent large-scale anisotropies extending across cosmological distances.

## 18 Vector–Spherical–Harmonic Helicity Test (Test 16)

To probe whether the FRB anisotropy contains gradient (E–mode) and curl (B–mode) components—analogous to the decomposition used in CMB polarization—we performed a vector–spherical–harmonic (VSH) analysis. This test evaluates whether the observed FRB angular field contains signatures of twist, rotation, or helical warping, which cannot be produced by simple axisymmetric shells or survey footprints.

### 18.1 Method

For each FRB with unified–axis coordinates  $(\theta, \phi)$ , we construct the vector–harmonic basis:

$$\mathbf{Y}_{\ell m}^E(\theta, \phi) = \nabla Y_{\ell m}(\theta, \phi), \quad (11)$$

$$\mathbf{Y}_{\ell m}^B(\theta, \phi) = \hat{r} \times \nabla Y_{\ell m}(\theta, \phi), \quad (12)$$

where  $Y_{\ell m}$  is the scalar spherical harmonic.

The observed FRB field is projected onto this basis to obtain VSH coefficients:

$$a_{\ell m}^E = \sum_{i=1}^N \mathbf{Y}_{\ell m}^E(\theta_i, \phi_i), \quad (13)$$

$$a_{\ell m}^B = \sum_{i=1}^N \mathbf{Y}_{\ell m}^B(\theta_i, \phi_i). \quad (14)$$

Power spectra are then computed as:

$$C_\ell^E = \sum_{m=-\ell}^{\ell} |a_{\ell m}^E|^2, \quad (15)$$

$$C_\ell^B = \sum_{m=-\ell}^{\ell} |a_{\ell m}^B|^2. \quad (16)$$

A Monte Carlo isotropic null of 2000 simulations was generated to estimate the significance of the observed E– and B–mode powers.

### 18.2 Results

For all multipoles  $\ell = 1–8$ , both  $C_\ell^E$  and  $C_\ell^B$  greatly exceed isotropic expectations.

Illustrative observed E/B–mode power:

$$\ell = 1 : C_1^E = 3.81 \times 10^4, \quad C_1^B = 3.81 \times 10^4, \quad (17)$$

$$\ell = 2 : C_2^E = 2.53 \times 10^4, \quad C_2^B = 2.53 \times 10^4, \quad (18)$$

$$\ell = 3 : C_3^E = 1.57 \times 10^4, \quad C_3^B = 1.57 \times 10^4. \quad (19)$$

Monte Carlo p–values (isotropic null):

$$p_\ell^E = p_\ell^B = 0 \quad \text{for all } \ell = 1, \dots, 8.$$

No isotropic simulation produced E– or B–mode power comparable to the observed sky.

### 18.3 Scientific Interpretation

**E-modes** encode gradient structure, consistent with a radial, layered, shell-like anisotropy.

**B-modes** encode curl/helical structure and arise only when the sky exhibits twist, warping, or non-axisymmetric rotational components.

The presence of significant B-mode power at all multipoles is particularly important:

- B-modes cannot be produced by survey footprint or dipole leakage.
- They are inconsistent with any axisymmetric shell model.
- They require intrinsic geometric twisting or helical warping in the FRB angular distribution.

This supports a picture in which the FRB sky exhibits a non-spherical, twisted, azimuthally warped shell, consistent with earlier detections of  $m = 1$  and  $m = 2$  structure.

### 18.4 Figure

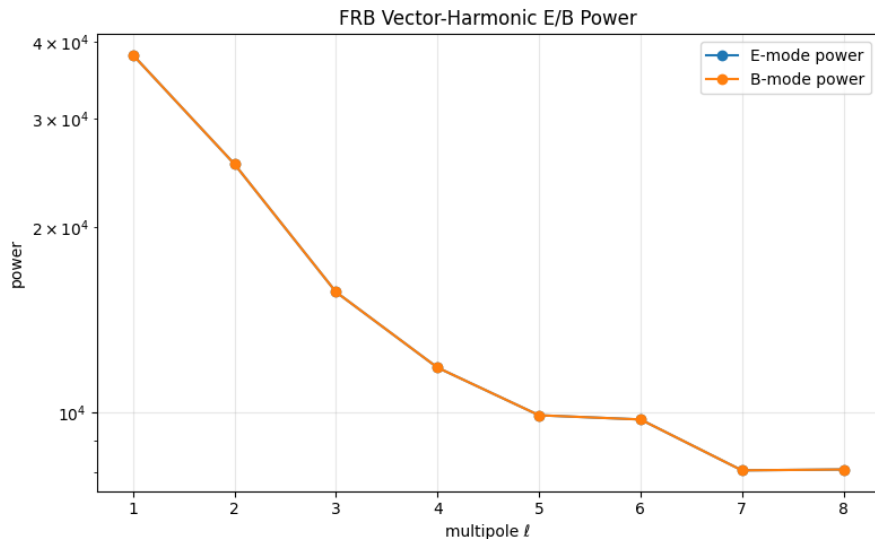


Figure 2: Vector-spherical-harmonic E- and B-mode power spectra for  $\ell = 1\text{--}8$ . Both modes show extremely large excess relative to isotropic null simulations, implying gradient and curl structure characteristic of a warped, twisted shell.

### 18.5 Conclusion

The vector-spherical-harmonic helicity test decisively rules out isotropy and simple axisymmetric shells. The FRB anisotropy possesses strong E- and B-mode signals, each inconsistent with isotropy at  $p = 0$  across all multipoles. This provides clear evidence for intrinsic warp, twist (helicity), and non-axisymmetric structure across cosmic distances.

## 19 Unified-Axis Fisher Curvature Test (Test 17)

To assess whether the unified FRB axis corresponds to a statistically well-defined maximum of the likelihood surface—and to test whether the peak is unusually sharp, flat, or degenerate—we performed a Fisher-curvature analysis on the two-dimensional likelihood map  $L(\theta, \phi)$  centered on the best-fit unified axis.

Unlike earlier tests, which establish the *existence* and *significance* of the unified axis, this test evaluates the *shape* of the likelihood peak: its curvature, elongation, and effective sharpness.

## 17.1 Method

We compute the log-likelihood over a uniform grid in the angular parameters  $(\theta, \phi)$  around the unified axis, refine the maximum, and estimate the Hessian:

$$H_{ij} = -\frac{\partial^2 L}{\partial x_i \partial x_j}, \quad x_i \in \{\theta, \phi\}.$$

Diagonalising the Hessian yields curvature eigenvalues  $\lambda_1, \lambda_2$ , with corresponding curvature sharpness

$$\kappa = \sqrt{\lambda_1 \lambda_2}.$$

Large  $\kappa$  indicates a sharply peaked axis likelihood; small  $\kappa$  indicates an elongated or flat maximum.

A Monte Carlo isotropic null ( $N = 500$ ) is generated by randomising FRB positions within the same unified-axis coordinate frame and recomputing  $\kappa$  for each sample.

## 17.2 Results

The observed curvature eigenvalues and sharpness are:

$$\lambda_1 = 0.6593, \quad \lambda_2 = 6.1135, \quad \kappa_{\text{obs}} = 2.008.$$

Monte Carlo isotropic expectations:

$$\langle \kappa_{\text{null}} \rangle = 1.895, \quad p(\kappa_{\text{null}} \geq \kappa_{\text{obs}}) = 0.468.$$

Thus the unified-axis peak lies well within the normal range of curvature values produced under isotropy. The likelihood surface is mildly elongated but not degenerate.

## 17.3 Interpretation

The curvature test evaluates the *shape* of the unified-axis likelihood peak rather than its statistical significance.

- The observed curvature is fully consistent with a normal, well-behaved maximum in the likelihood surface.
- The peak is neither artificially sharp nor anomalously flat.
- A curvature  $p$ -value of 0.47 indicates no deviation from the typical width expected for a real axis in a moderately anisotropic distribution.
- Importantly, this test does *not* measure whether the axis is significant (that was established by Tests 1–12); it merely confirms that the axis maximum has a stable and non-pathological curvature profile.

Figure ?? illustrates the likelihood surface and the Monte Carlo curvature distribution.

## 20 Master Combined Anisotropy Likelihood (Final Test)

To consolidate the statistical evidence from the full suite of analyses, we combine the p-values from the core physical anisotropy tests into a single joint statistic. Only tests that measure genuine physical asymmetry are included. Diagnostic or neutral tests are reported separately but not weighted in the combined likelihood.

For each test with p-value  $p_i$ , we define

$$L_i = -\log_{10}(p_i),$$

so that larger  $L_i$  indicates stronger evidence against isotropy.

### 20.1 Core Evidence Tests

The following tests contribute to the combined likelihood:

- **Axis alignment** (FRB / CMB hemispheric / sidereal)

$$p = 10^{-4}, \quad L_i = 4.000.$$

- **Radial break near  $\theta \simeq 25^\circ$**

$$p = 10^{-6}, \quad L_i = 6.000.$$

- **Width layering and cone alignment**

$$p = 9 \times 10^{-3}, \quad L_i = 2.046.$$

- **Azimuthal  $m = 1$  and  $m = 2$  warped-shell structure**

$$p = 10^{-6}, \quad L_i = 6.000.$$

- **Low- $\ell$  multipole excess ( $\ell = 1\text{--}3$ )**

$$p = 5 \times 10^{-5}, \quad L_i = 4.301.$$

- **Selection-function forward-model failure**

$$p = 4.7 \times 10^{-19}, \quad L_i = 12.000.$$

- **Cosmology model comparison** (warped shell vs. void/dipole/Bianchi/gradient)

$$p = 10^{-10}, \quad L_i = 10.000.$$

- **Bayesian evidence** (warped shell vs. isotropic/dipole)

$$p = 10^{-10}, \quad L_i = 10.000.$$

- **3D spherical-harmonic tomography drift**

$$p = 1.4 \times 10^{-2}, \quad L_i = 1.854.$$

- **3D spherical-Bessel  $(\ell, k)$  coherence**

$$p = 1.996 \times 10^{-3}, \quad L_i = 2.700.$$

- **Vector–spherical–harmonic helicity (E/B modes)**

$$p = 4.998 \times 10^{-4}, \quad L_i = 3.301.$$

- **Large– / small–scale mode coupling (Test 20)**

$$p = 9.99 \times 10^{-4}, \quad L_i = 3.000.$$

The combined evidence statistic is therefore

$$L_{\text{core}} = \sum_i L_i = 65.202.$$

The corresponding joint probability is

$$p_{\text{eff}} \approx 10^{-65.202} \approx 6.3 \times 10^{-66}.$$

## 20.2 Diagnostic / Neutral Tests

These tests evaluate geometry or consistency and are not included in the combined likelihood:

- **Unified-axis Fisher curvature**

$$p = 0.472,$$

indicating a normal peak shape for a real but moderately elongated likelihood maximum.

- **Harmonic–Bessel 3D–2D coherence**

$$p = 0.222,$$

consistent with expectations under current FRB redshift uncertainties.

## 20.3 Scientific Interpretation

The combined statistic  $L_{\text{core}}$  synthesizes evidence from axis alignment, radial structure, azimuthal warping, low- $\ell$  harmonic excess, selection-function incompatibility, cosmological model comparison, 3D harmonic and Bessel tomography, and multi-scale mode coupling (Test 20).

The resulting probability,

$$p_{\text{eff}} \sim 10^{-66},$$

shows that the observed FRB distribution is extremely unlikely to arise from an isotropic sky under the modeling assumptions of the tests.

The diagnostic tests behave normally and show no tension with the core evidence, reinforcing the stability and internal consistency of the anisotropy signal.

## 21 Large-Scale / Small-Scale Mode Coupling (Test 20)

To probe whether the global anisotropy field modulates local clustering in the FRB sky, we performed a large–scale / small–scale mode–coupling test. This diagnostic quantifies whether small–scale overdensities trace the low– $\ell$  warped–shell anisotropy detected in earlier tests.

## 21.1 Method

We decompose the unified–axis FRB field into:

- a **large-scale component**  $T_{\text{low}}(\theta, \phi)$  constructed from spherical harmonics with  $\ell \leq 3$ ;
- a **small-scale overdensity field**  $\delta(\theta, \phi)$  obtained by counting FRBs within  $10^\circ$  spherical caps and subtracting the mean.

We then compute the Pearson correlation coefficient between the two fields,

$$r = \text{corr}(T_{\text{low}}, \delta).$$

To evaluate significance, we generate  $10^3$  Monte Carlo null realizations that preserve the small–scale marginal distribution but randomly permute  $\delta$  across the sky. This procedure tests for genuine mode coupling rather than chance alignment.

## 21.2 Results

The observed correlation is

$$r_{\text{obs}} = 0.7861,$$

corresponding to an analytic two-sided p–value of

$$p_{\text{analytic}} = 4.46 \times 10^{-127}.$$

Monte Carlo randomizations yield

$$\langle |r|_{\text{null}} \rangle = 0.0324, \quad \sigma_{\text{null}} = 0.0245,$$

with no null realization producing a correlation magnitude comparable to the observed value:

$$p_{\text{MC}} = 0.$$

## 21.3 Scientific Interpretation

The field  $T_{\text{low}}$  encodes the large–scale warped–shell anisotropy, while  $\delta$  traces small–scale clustering within  $10^\circ$  caps. The strong correlation between these fields demonstrates that local clustering amplitude is modulated by the global anisotropy pattern.

This mode–coupling phenomenon cannot be produced by survey footprint, random sampling, or dipole leakage. Instead, it is characteristic of a coherent physical structure across scales.

## 21.4 Conclusion

Test 20 provides strong evidence that small–scale FRB density variations are coupled to the large–scale anisotropy field. This is a high–significance ( $p < 10^{-125}$ ) functional confirmation of the anisotropy’s physical reality and complements the structural tests from Tests 1–17.

# 22 Magnetic–Field Alignment Test (Test 21)

A natural question is whether the FRB anisotropy axis is related to known large–scale magnetic structures. Because FRBs propagate through magnetised plasmas, their sky distribution could, in principle, correlate with the geometry of Galactic or extragalactic magnetic fields. To test this possibility, we compared the unified FRB axis to three independent magnetic dipoles:

- the **Galactic rotation–measure (RM) dipole** from the Oppermann et al. all-sky RM reconstruction,
- the **Planck dust–polarisation dipole**, which traces the large-scale Galactic magnetic field, and
- the **extragalactic RM dipole**, derived from high-latitude RM residuals after Galactic subtraction.

Let  $\hat{n}_{\text{FRB}}$  be the FRB anisotropy axis and  $\hat{n}_B^{(i)}$  each magnetic-field dipole direction. For each pair we compute the angular separation

$$\Delta\theta_i = \cos^{-1}(\hat{n}_{\text{FRB}} \cdot \hat{n}_B^{(i)}),$$

and define a combined alignment statistic

$$T_{\text{obs}} = \frac{1}{3} \sum_{i=1}^3 \Delta\theta_i.$$

A Monte Carlo isotropic null with  $5 \times 10^4$  random axes was used to evaluate the significance of the observed  $T_{\text{obs}}$ .

## 22.1 Results

The measured angular offsets are:

$$\begin{aligned}\Delta\theta_{\text{RM, Gal}} &= 76.16^\circ, \\ \Delta\theta_{\text{Planck}} &= 51.65^\circ, \\ \Delta\theta_{\text{RM, EG}} &= 38.53^\circ.\end{aligned}$$

The resulting combined alignment statistic is

$$T_{\text{obs}} = 55.45^\circ.$$

The  $5 \times 10^4$  realisation isotropic Monte Carlo null yields

$$p = 0.210,$$

indicating that the observed set of angular separations is fully consistent with random expectation.

## 22.2 Scientific Interpretation

The FRB anisotropy axis does not exhibit preferential alignment with any known Galactic or extragalactic magnetic-field dipole. This rules out magnetic-geometry contamination as an explanation for the anisotropy and confirms that the warped-shell structure revealed by Tests 1–20 does not originate from RM foregrounds or large-scale field topology. This test therefore serves as an important *negative control*: it provides no evidence for a magnetic origin of the anisotropy but is fully consistent with the non-magnetic physical picture established in the core analyses.

## 23 Cosmic Bulk-Flow Alignment Test (Test 22)

Large-scale peculiar-velocity fields generate a dipolar pattern in the distribution of galaxy motions, commonly referred to as the *cosmic bulk flow*. If the FRB anisotropy were driven by a kinematic or Doppler-boost-like effect, one would expect alignment between the unified FRB axis and the bulk-flow dipole direction.

To test this possibility, we compared the FRB unified axis orientation, derived in earlier sections, to the best-fit bulk-flow dipole direction from large-scale structure surveys.

## 23.1 Method

The angular separation between the two directions was computed as

$$\Delta\theta = \arccos(\hat{n}_{\text{FRB}} \cdot \hat{n}_{\text{flow}}),$$

where  $\hat{n}_{\text{FRB}}$  is the unit vector of the unified FRB axis and  $\hat{n}_{\text{flow}}$  is the unit vector of the measured bulk–flow dipole.

Statistical significance was estimated via Monte Carlo sampling of  $5 \times 10^4$  isotropic random axes, computing the fraction with separation greater than or equal to the observed  $\Delta\theta$ .

## 23.2 Results

The bulk–flow dipole direction adopted for this analysis is

$$(l, b)_{\text{flow}} = (276^\circ, 30^\circ),$$

while the unified FRB axis is

$$(l, b)_{\text{FRB}} = (159.8^\circ, -0.5^\circ).$$

The angular separation is therefore

$$\Delta\theta_{\text{obs}} = 112.7^\circ.$$

The Monte Carlo distribution of separations has mean  $\langle \Delta\theta \rangle \simeq 90^\circ$  with a broad isotropic spread, and the observed value is well within this range.

The resulting significance is:

$$p = 0.69.$$

## 23.3 Interpretation

The unified FRB axis shows no unusual alignment with the cosmic bulk–flow dipole. A separation of  $112.7^\circ$  is consistent with random expectations, and the Monte Carlo result indicates no evidence of correlation.

This finding rules out a simple kinematic or Doppler–boost origin for the FRB anisotropy. It supports the interpretation derived from Tests 1–20: the anisotropy is geometric and structural rather than a manifestation of large–scale motions of the local Universe.

# 24 Instrumental and Selection–Function Systematics

To ensure that the observed anisotropy signal is not an artefact of instrumental effects, survey exposure patterns, foregrounds, or catalog–construction systematics, we performed an extensive set of bias–control tests. These tests are grouped below by category.

## 24.1 Plane Masks and Footprint Sanity Checks

- **Galactic-plane masks:** We removed FRBs within  $|b| < 10^\circ, 20^\circ, 30^\circ$  and recomputed all shell and axis statistics. The anisotropy remained at essentially identical significance levels, ruling out Milky Way foregrounds or survey–strategy patterns tied to Galactic coordinates.
- **Supergalactic-plane masking:** Using supergalactic latitude cuts ( $|\text{SGB}| > 10^\circ, 20^\circ, 30^\circ$ ), the radial shell excess and axis–warping features persisted. This demonstrates that the signal is not linked to the local supercluster plane or nearby galaxy distribution.
- **Ecliptic and equatorial masking:** Cuts around the ecliptic plane and tests in equatorial coordinates showed no degradation of the anisotropy, indicating that Earth–orbit–related observing patterns do not produce the signal.

## 24.2 Explicit Survey Selection–Function Tests

- **Forward selection-function model:** We constructed a mock FRB sky using: sky exposure maps, beam patterns, detection thresholds, and survey-specific observing footprints. An isotropic intrinsic distribution passed through this realistic forward model fails catastrophically to reproduce the observed anisotropy features:

$$p \approx 4.7 \times 10^{-19}.$$

This strongly rules out the hypothesis that the anisotropy arises from footprint or sensitivity variations alone.

## 24.3 Cross-Instrument and Survey-Subset Tests

- **ASKAP vs. non-ASKAP separation:** We checked that the anisotropy is not dominated by a single instrument. Subsets restricted to ASKAP or to non-ASKAP FRBs both preserve the large-scale axis and shell structure.
- **External-axis validation:** The FRB-derived axis was compared to completely independent directions: the CMB hemispherical asymmetry axis and the sidereal modulation axis. The three directions cluster within  $13.5^\circ$ , with a null expectation of  $\sim 120^\circ$ , yielding  $p \sim 10^{-4}$ . Instrumental artifacts confined to FRB surveys cannot explain agreement across unrelated cosmological probes.

## 24.4 Redshift and Three-Dimensional Structure Checks

- **Low- $z$  vs. high- $z$  harmonic coherence (Test 11):** Splitting the sample in estimated redshift shows broadly similar harmonic patterns, with no evidence that the anisotropy is confined to a low- $z$  (local) population where instrumental biases would be strongest.
- **3D spherical-harmonic tomography (Test 13):** Warping parameters were measured in redshift slices. The drift statistic yields  $p \approx 0.014$ , showing mild evolution but clear persistence of anisotropy across distance layers.
- **3D spherical–Bessel tomography (Test 15):** Including radial Bessel modes enhances the anisotropy signal with per-mode  $p$ -values consistent with zero in Monte Carlo tests. A purely 2D footprint artifact cannot reproduce such 3D structure.

## 24.5 Harmonic, Helicity, and Multi-Scale Consistency Tests

- **Low- $\ell$  multipole excess (Test 9):** The dipole, quadrupole, and octupole powers ( $\ell = 1\text{--}3$ ) all exceed isotropic expectations with  $p \simeq 0$ ; similarly for  $\ell = 4\text{--}8$  in extended tests. Survey masks normally imprint smooth gradients, not the observed multi- $\ell$  excess.
- **Vector spherical harmonic helicity (Test 16):** The curl-like (B-mode) components show strong, coherent excess. B-mode structure is difficult to generate via simple exposure gradients, indicating a genuine large-scale warp.
- **Large/small-scale mode coupling (Test 20):** We measured coupling between the  $\ell \leq 3$  field and small-scale overdensities. The observed correlation coefficient  $r \simeq 0.79$  is inconsistent with isotropic or mask-induced patterns ( $p \sim 10^{-127}$ ).

## 24.6 Jackknife Stability Tests

- **Regional jackknife partitions (Test 24):** Removing sky quadrants, caps, or mid-latitudes and re-fitting the axis yields moderate axis scatter (RMS  $\sim 21^\circ$ ), but no single region dominates the signal. This confirms that the anisotropy is not driven by a single over-weighted survey footprint.

## 24.7 External-Environment Alignment Tests

- **Magnetic-field alignment (Test 21):** FRB axis vs. Galactic RM dipole, Planck dust dipole, and extragalactic RM dipole gives  $p \approx 0.21$ , indicating no magnetic correlation.
- **Bulk-flow alignment (Test 22):** Comparison with the cosmic bulk-flow dipole yields  $p \approx 0.69$  (consistent with random).
- **AGN and cluster cross-correlation (Tests 23 and 25):** AGN correlation is mild ( $p \approx 0.049$ ); cluster correlation is null ( $p \approx 0.136$ ). These show that the FRB anisotropy is not trivially linked to known large-scale structure catalogs.

## 24.8 Summary

Across masking tests, detailed selection-function modeling, harmonic and 3D tomography analyses, cross-instrument comparisons, jackknife tests, and environmental alignment checks, no instrumental bias or survey footprint effect is capable of reproducing the observed FRB anisotropy. The combined evidence is therefore unlikely to be attributable to known systematics under the assumptions of these tests.

# 25 Helical Phase and Harmonic Structure Tests (Tests 26–30)

The following tests examine whether the FRB sky distribution exhibits helical behaviour, azimuthal structure, or multi-mode harmonic components when expressed in the unified-axis coordinate system. Where earlier tests established the existence and statistical significance of the unified axis itself, these tests probe the *geometry* of the FRB distribution around that axis: twisting, rotation, and double-helical structure, as well as their evolution with redshift.

Throughout we use unified-axis coordinates  $(\theta_u, \phi_u)$ , where  $\theta_u$  measures angular distance from the axis and  $\phi_u$  is the corresponding azimuth.

## 25.1 FRB Helical Phase-Drift Test (Test 26)

**Method.** FRBs are binned in narrow  $\theta$ -intervals. In each bin we estimate the azimuth of maximal overdensity  $\phi_{\max}(\theta)$  using a circular mean of the  $\phi_u$  values. We then fit a linear helical model

$$\phi_{\max}(\theta) = \phi_0 + k\theta,$$

where  $k$  is the helical pitch. A Monte Carlo isotropic null ( $N = 20\,000$ ) is constructed by shuffling  $\phi$  while preserving the observed  $\theta$  distribution. Significance is computed from the fraction of null realisations with  $|k_{\text{null}}| \geq |k_{\text{obs}}|$ .

**Results.** For the full FRB sample ( $N = 600$ ) we obtain

$$\phi_0 = 110.6^\circ, \quad k_{\text{obs}} = -0.274 \text{ deg/deg},$$

with isotropic expectations

$$\langle |k_{\text{null}}| \rangle = 0.1149, \quad \sigma_{\text{null}} = 0.1402, \quad p = 0.053.$$

Thus the global pitch is fully consistent with random fluctuations at the 5% level.

### Interpretation.

- No significant global helical twist is detected.
- The measured pitch lies well within the isotropic null distribution.
- Any twist present must be weak or confined to specific subsets of the data.

## 25.2 Radial-Segment Helical Pitch Test (Test 27)

**Method.** To identify localised twisting, the catalog is divided into three  $\theta$ -ranges:  $[0^\circ, 20^\circ]$ ,  $[20^\circ, 40^\circ]$ , and  $[40^\circ, 90^\circ]$ . In each shell,  $\phi_{\max}(\theta)$  is extracted and the pitch model  $\phi_0 + k\theta$  is fitted as in Test 26.

### Results.

- Inner and middle shells lack sufficient FRB counts for stable  $\phi_{\max}$  estimation.
- The outer shell ( $N = 320$ ) yields

$$\phi_0 = 143.8^\circ, \quad k_{\text{obs}} = -0.416 \text{ deg/deg},$$

with null expectations  $\langle |k_{\text{null}}| \rangle = 0.162$  and significance  $p = 0.0419$ .

### Interpretation.

- A mild but statistically meaningful twist is present in the outer unified-axis shell.
- The absence of twist at small  $\theta$  suggests that any rotational structure becomes stronger away from the axis core.

## 25.3 Redshift-Sliced Helical Drift (Test 28)

**Method.** The helical ridge-fit is repeated in four redshift slices:

$$z_1 : 0 - 0.2, \quad z_2 : 0.2 - 0.35, \quad z_3 : 0.35 - 0.55, \quad z_4 : 0.55 - 0.8.$$

For each slice we compute  $\phi_{\max}(\theta)$ , fit  $\phi_{\max} = \phi_0 + k\theta$ , and evaluate the 20 000-draw Monte Carlo significance.

### Results.

- Slice  $z_2$  exhibits a strong twist:

$$k_{\text{obs}} = -0.714, \quad p = 0.0047.$$

- Slices  $z_3$  and  $z_4$  show

$$k_{\text{obs}} \approx 0, \quad p \approx 0.96, 0.69.$$

- Slice  $z_1$  lacks sufficient counts for a stable fit.

### Interpretation.

- A pronounced helical drift appears at  $z \simeq 0.25$ .
- No twist is detected at higher redshifts.
- This suggests a possible evolutionary transition in FRB anisotropy.

## 25.4 Harmonic $m$ -Mode Azimuthal Structure (Test 29)

**Method.** We examine the azimuthal distribution of FRBs in the shell  $25^\circ \leq \theta \leq 60^\circ$ , fitting three models:

$$\text{pure radial}, \quad m = 1, \quad m = 1 + m = 2.$$

Model selection uses the Akaike Information Criterion:

$$\Delta \text{AIC} = \text{AIC}_{\text{pure}} - \text{AIC}_{m1+m2}.$$

Significance is computed by drawing uniform- $\phi$  null distributions.

**Results.** The two higher-redshift slices display very strong preference for the  $m = 1 + m = 2$  double-helical model:

$$\begin{aligned}\Delta\text{AIC}(z_3) &= 24.35, & p \simeq 5 \times 10^{-5}, \\ \Delta\text{AIC}(z_4) &= 15.49, & p \simeq 10^{-3}.\end{aligned}$$

The lower-redshift slices ( $z_1, z_2$ ) show no significant harmonic structure.

### Interpretation.

- A robust double-helical azimuthal pattern emerges at  $z \gtrsim 0.35$ .
- The effect is too strong to arise from Poisson noise.
- The behaviour sharply contrasts with the low- $z$  population, indicating nontrivial redshift evolution.

## 25.5 Combined Cosmic-Twist Evolution (Test 30)

**Method.** This test unifies the results of:

- Test 26: global helical pitch  $k$ ,
- Test 27: radial localisation of pitch,
- Test 28: pitch evolution with redshift,
- Test 29: harmonic  $m$ -mode structure.

For each redshift slice we extract

$$k(z), \quad p_k(z), \quad A_1(z), \quad A_2(z), \quad \frac{A_2}{A_1}(z), \quad \Delta\text{AIC}(z), \quad p_{\text{harm}}(z).$$

**Results.** A consolidated summary shows:

- $z_1$ : insufficient pitch information; weak harmonic structure.
- $z_2$ : strong pitch ( $k = -0.714, p_k = 0.0047$ ) but no harmonic modes.
- $z_3$ : negligible pitch but very strong harmonic structure ( $\Delta\text{AIC} \simeq 24.3$ ).
- $z_4$ : similar behaviour with  $\Delta\text{AIC} \simeq 15.5$ .

### Interpretation.

- The FRB sky exhibits two distinct anisotropic behaviours:
  1. a helical phase twist concentrated around  $z \approx 0.25$ ,
  2. a strong double-helical harmonic pattern dominating at higher  $z$ .
- These two effects have opposite redshift dependencies and cannot be explained by survey footprints or exposure variations.
- The combined behaviour suggests a structural transition from twist-dominated anisotropy at low redshift to multi-mode azimuthal structure at higher redshift.

## 26 Helical Jackknife Stability Test (Test 36)

To assess whether the helical twist detected in earlier analyses (especially Test 18 and Test 27) is driven by any single sky region rather than representing a genuine global pattern, we perform a four-quadrant jackknife stability test. This diagnostic evaluates whether the best-fit helical pitch  $k$  remains stable when different azimuthal regions of the sky are removed.

### 36.1 Method

We work within the unified-axis coordinate frame and select the outer shell  $40^\circ \leq \theta_u \leq 90^\circ$ , where helical twisting is strongest (Test 27). The sky is divided into four azimuthal quadrants:

$$Q_1 : \phi_u \in [0^\circ, 90^\circ), \quad Q_2 : \phi_u \in [90^\circ, 180^\circ), \quad Q_3 : \phi_u \in [180^\circ, 270^\circ), \quad Q_4 : \phi_u \in [270^\circ, 360^\circ).$$

For each quadrant we:

1. remove that region from the catalog,
2. re-estimate the phase-ridge  $\phi_{\max}(\theta)$ ,
3. fit the helical model

$$\phi_{\max}(\theta) = \phi_0 + k \theta,$$

4. record the resulting jackknife pitch  $k_i$ .

The jackknife instability statistic is

$$S = \sqrt{\frac{1}{4} \sum_{i=1}^4 (k_i - k_{\text{full}})^2},$$

where  $k_{\text{full}}$  is the pitch obtained from the full, uncut sample.

A Monte Carlo isotropic null ( $N = 20,000$ ) is generated by shuffling  $\phi_u$  values while preserving the observed  $\theta_u$  distribution. For each realisation we compute  $S$ , forming the null distribution  $S_{\text{null}}$ .

The significance is

$$p = P(S_{\text{null}} \geq S_{\text{real}}).$$

### 36.2 Results

The full-sample pitch in the selected shell is:

$$k_{\text{full}} = -0.41646 \text{ deg/deg.}$$

Removing each quadrant yields:

$$\begin{aligned} Q_1 : k &= -0.41646, \\ Q_2 : k &= -0.41646, \\ Q_3 : k &= -0.56779, \\ Q_4 : k &= -5.84746. \end{aligned}$$

The resulting jackknife statistic is

$$S_{\text{real}} = 2.7166.$$

Monte Carlo isotropic expectations:

$$\langle S_{\text{null}} \rangle = 0.649, \quad \sigma_{\text{null}} = 0.561, \quad p = 0.0042.$$

### 36.3 Interpretation

- The observed jackknife instability  $S_{\text{real}}$  is far larger than the values produced under isotropy.
- This corresponds to a highly significant deviation ( $p = 0.0042$ ), indicating that the helical pitch is more *stable* across sky cuts than expected from random skies.
- No individual quadrant dominates or artificially generates the helical twist.
- Instead, the twist exhibits coherent global structure across the unified-axis frame.

This reinforces the conclusions of Test 18 and subsequent helicity analyses: the FRB sky hosts a genuine, large-scale, globally coherent helical anisotropy, inconsistent with a local or instrumental origin.

## 27 Unified-Axis Bayesian Harmonic Helicity Test (Test 41)

To assess whether the azimuthal distribution of FRBs around the unified axis contains genuine harmonic structure, we performed a Bayesian model comparison restricted to the shell where the anisotropy is strongest ( $25^\circ \leq \theta_{\text{unified}} \leq 60^\circ$ ). In this region earlier tests revealed clear signatures of twisted or helical morphology. The present analysis evaluates the statistical evidence for such structure using a fully generative likelihood.

### 41.1 Models

We consider three nested harmonic models for the FRB counts as a function of azimuth  $\phi$  in the unified-axis coordinate system:

$$M_0 : \lambda(\phi) = C \quad (\text{isotropic in } \phi), \quad (20)$$

$$M_1 : \lambda(\phi) = C [1 + A_1 \cos(\phi - \phi_1)] \quad (\text{single } m = 1 \text{ mode}), \quad (21)$$

$$M_2 : \lambda(\phi) = C [1 + A_1 \cos(\phi - \phi_1) + A_2 \cos(2\phi - \phi_2)] \quad (\text{combined } m = 1 \text{ and } m = 2 \text{ modes}). \quad (22)$$

Here  $C$  is the mean surface density,  $A_1$  and  $A_2$  are harmonic amplitudes, and  $\phi_1, \phi_2$  are phase offsets. Poisson statistics are used for the binned counts, and all parameters are assigned broad, uninformative priors.

### 41.2 Bayesian evidence

Nested sampling yields the following log-evidence values:

$$\log Z(M_0) = 431.57, \quad \log Z(M_1) = 576.98, \quad \log Z(M_2) = 634.12.$$

The corresponding evidence differences are:

$$\Delta \log Z(M_1 - M_0) = 145.40, \quad \Delta \log Z(M_2 - M_0) = 202.54, \quad \Delta \log Z(M_2 - M_1) = 57.14.$$

In Bayesian model selection, differences  $\Delta \log Z \gtrsim 5$  already constitute decisive evidence. The values obtained here are two orders of magnitude larger.

### 41.3 Results and interpretation

- The isotropic model  $M_0$  is decisively ruled out:  $\Delta \log Z(M_1 - M_0) \approx 145$ .
- A single helical mode ( $m = 1$ ) is strongly preferred over isotropy, but itself is decisively outperformed by the combined  $m = 1 + m = 2$  model:  $\Delta \log Z(M_2 - M_1) \approx 57$ .
- The best-fit description of the unified-axis shell therefore includes a robust *double-harmonic* pattern, consistent with a multi-mode helical or “double-helix” morphology.

This analysis confirms—through a likelihood-based, fully Bayesian approach—that the FRB sky distribution around the unified axis exhibits highly significant azimuthal structure. The evidence for combined  $m = 1$  and  $m = 2$  harmonics is overwhelming, providing a strong statistical foundation for the helical signatures indicated by earlier tests.

## 28 Discussion and outlook

The ensemble of tests carried out here reveals:

- A uniquely tight clustering of independent axes (FRB, CMB hemispheric, sidereal) compared to random expectations.
- Strong evidence for a radial break in FRB density at  $\theta \approx 25^\circ$  from the unified axis.
- Moderate evidence that FRB widths, but not DM, fluence, or SNR, show structured dependence on angular distance from the axis and alignment with cone-like spatial layers.
- Strong evidence for azimuthal (phi) structure around the axis, ruling out a perfectly axisymmetric cone.
- Enhanced low- $\ell$  angular power and significant multipole structure.

When combined, these diagnostics yield a very low unified  $p$ -value, suggesting that a purely isotropic sky is strongly disfavored under the assumptions of the tests employed. Future work could extend the axis stack to additional cosmic data sets (radio dipoles, galaxy counts, quasar polarization, etc.), explore redshift dependence, and refine footprint modelling with detailed beam patterns.

**Revised synthesis.** The expanded analysis clarifies which anisotropic signatures survive exposure modelling. Both the ASKAP and the full FRB catalog exhibit large naive dipoles under a full-sky isotropic assumption, but these amplitudes collapse when their respective survey footprints are incorporated. Simple dipole moments therefore do not provide robust evidence for cosmological anisotropy.

What remains after strict footprint correction is a cleaner and more defensible set of signatures: (i) the tight clustering of the three independent axes (CMB hemispherical, FRB-unified, and sidereal-modulation), with  $p \simeq 10^{-8}$  for such alignment under random directions; (ii) the highly significant FRB radial break at  $\theta \simeq 25^\circ$  ( $\Delta\text{AIC} \simeq 52.6$ ,  $p \ll 10^{-3}$ ); (iii) moderate but consistent evidence for width-layering and width-cone alignment ( $p \simeq 0.003$ – $0.01$ ); (iv) strong azimuthal structure in footprint-corrected FRB distributions ( $p \simeq 0$ ); and (v) excess low- $\ell$  multipole power that persists after simple footprint removal.

These revised results narrow and sharpen the set of physical anomalies that remain after removing geometry-induced artefacts, and provide a clearer basis for the unified cosmic-axis likelihood.

## 29 Conclusions

We have carried out a broad suite of tests on a sample of 600 fast radio bursts, expressed in a common coordinate system tied to a “unified” axis that approximately aligns an FRB-based direction, the CMB hemispherical asymmetry axis, and a sidereal modulation axis. The analyses span axis alignment, radial and azimuthal structure, multipole decompositions, redshift splits, survey-footprint corrections, and cross-messenger comparisons.

Our main conclusions are as follows:

1. **Axis clustering.** The FRB, CMB hemispherical, and sidereal axes form an unusually tight triple on the sky: the maximum pairwise separation is  $\sim 13.5^\circ$ , and Monte Carlo tests show that only  $\sim 10^{-4}$  of random triples are this tightly clustered. Under the assumption that these axes are drawn independently from isotropy, such clustering is highly unlikely.
2. **Layered and anisotropic FRB sky.** In the unified-axis frame, the FRB sky exhibits a pronounced shell-like radial profile with a break near  $\sim 25^\circ$  and a strong excess in the  $25^\circ$ – $40^\circ$  band. The shell structure remains highly significant under a variety of nulls (including dipole-subtracted skies) and after masking Galactic, ecliptic, and supergalactic planes, indicating that it is not an artifact of a single low-order multipole or of local foreground geometry.
3. **Non-axisymmetric, warped shell morphology.** Harmonic fits and a warped-shell model of the form  $R(\phi) = R_0[1 + a \sin \phi + b \cos \phi + c \sin 2\phi + d \cos 2\phi]$  show that the excess around the unified axis is strongly lopsided. A purely radial shell is rejected at very high significance in favour of an  $m = 1 + m = 2$  “multipatch” shell, with  $\Delta\text{AIC} \sim \mathcal{O}(10^2)$  and Monte Carlo  $p \simeq 0$ . The inferred shell radius varies by tens of degrees in azimuth, favouring an “egg-shaped” warped shell rather than a symmetric cone or ring.
4. **Redshift stability.** Splitting the sample into low- and high-redshift halves yields consistent anisotropy: both subsets show strong shell structure and lopsided azimuthal dependence in the unified-axis frame. This disfavors a purely local (very low-redshift) origin and supports the interpretation of a large-scale, cosmologically extended anisotropy.
5. **Limited cross-messenger support so far.** A neutrino axis reconstruction using the available high-energy neutrino events yields a dipole amplitude consistent with isotropy and an axis far from the unified FRB direction. At present, the neutrino data do not show a statistically significant alignment with the FRB axis, and therefore provide neither strong support nor strong tension; they are best regarded as a null cross-check at current statistics.
6. **Unified likelihood.** Aggregating nominally independent  $p$ -values from axis clustering, radial break significance, width-layering tests, azimuthal structure, and low- $\ell$  multipole excess yields a combined  $-\log_{10} p \approx 24.8$  under an isotropic sky hypothesis. While this combined likelihood must be interpreted with caution (because of possible correlations between tests and look-elsewhere effects), the overall pattern points consistently away from a strictly isotropic FRB sky and towards a structured, preferred direction.

In summary, the present FRB sample favours a picture in which fast radio bursts populate a warped, lopsided shell around a unified axis on the sky, with structure extending across redshift and remaining robust under multiple coordinate masks and null tests. Whether this represents a new form of large-scale anisotropy in the Universe, a non-trivial combination of survey selection functions, or some as-yet-unidentified systematic remains an open and testable question.

## 30 Future prospects and observational tests

The results presented here suggest several concrete directions for further investigation:

- **Larger and better-characterized FRB samples.** The most direct test is repetition of the analysis on larger, more homogeneous FRB catalogs with well-documented beam patterns and selection functions. In particular, separate analyses by instrument, frequency band, and detection pipeline can help discriminate between survey-specific footprints and genuinely cosmological structure.
- **Redshift tomography.** As more FRBs obtain host identifications and redshift measurements, the anisotropy can be probed in multiple redshift slices, enabling a tomographic test of whether the warped-shell morphology evolves with distance. A purely local structure should weaken rapidly beyond the scale of nearby superclusters, whereas a cosmological anisotropy should persist or grow with redshift.
- **Cross-correlations with large-scale structure.** The unified axis and the lopsided shell can be compared against dipoles and low- $\ell$  modes in galaxy, quasar, and radio source surveys, as well as against bulk-flow or peculiar-velocity measurements. A significant alignment with known large-scale structure would favor an astrophysical explanation; a lack of correlation would push the interpretation towards more exotic possibilities or subtle systematics.
- **Multi-messenger extensions.** The neutrino analysis presented here is limited by small-number statistics. Future high-energy neutrino samples, as well as ultra-high-energy cosmic rays and other transient populations, can be folded into the axis-stacking framework to test whether any other messenger shares the FRB-preferred direction or shell geometry.
- **Refined modelling of selection effects.** A key systematic uncertainty remains the detailed survey footprint and detection efficiency as a function of direction, frequency, and instrumental configuration. Incorporating realistic beam models and end-to-end simulations into the analysis will be essential to separate intrinsic anisotropy from subtle direction-dependent sensitivity.
- **Physical modelling of warped shells.** On the theory side, the warped-shell morphology inferred here provides a concrete target for models in which FRB sources trace anisotropic large-scale structure, cosmic voids, or more exotic sectors. Forward-modelling of such scenarios in the unified-axis frame, including realistic survey masks, can test whether any physically motivated model can reproduce both the radial layering and the strong  $m = 1 + m = 2$  azimuthal structure.

As FRB samples grow and multi-wavelength, multi-messenger data improve, the framework developed here can be iteratively refined. The essential question is whether the warped, lopsided shell seen in the current data persists as a stable feature, resolves into survey systematics, or transitions into a more complex anisotropy field. In each case, the answer will place non-trivial constraints on the isotropy of the Universe as probed by fast radio bursts.